

1 **Base metal sulphide geochemistry of southern African**
2 **mantle eclogites (Roberts Victor): Implications for cratonic**
3 **mafic magmatism and metallogenesis**

4
5 **Hannah S.R Hughes^{1,8*}, Charlie Compton-Jones¹, Iain McDonald², Ekaterina S. Kiseeva^{3,4}, Vadim S.**
6 **Kamenetsky^{5,6}, Gavyn Rollinson¹, Judith A. Coggon⁷, Judith A. Kinnaird^{1,8}, Grant M. Bybee⁸**

7 ¹Camborne School of Mines, University of Exeter, Cornwall Campus, Penryn, Cornwall, TR10 9FE, UK

8 ²School of Earth and Ocean Sciences, Cardiff University, Main Building, Cardiff CF10 3AT, UK

9 ³Department of Earth Sciences, University of Oxford, Oxford, OX1 3AN, UK

10 ⁴School of Biological, Earth and Environmental Sciences, University College Cork, Cork, Ireland

11 ⁵ARC Centre of Excellence in Ore Deposits and School of Earth Sciences, University of Tasmania,
12 Hobart, TAS 7001, Australia

13 ⁶Institute of Experimental Mineralogy, Chernogolovka, Russia

14 ⁷School of Ocean and Earth Science, University of Southampton, Waterfront Campus, European Way,
15 Southampton SO14 3ZH, UK

16 ⁸School of Geoscience, University of the Witwatersrand, Johannesburg, South Africa

17
18
19 *Corresponding author email: h.hughes@exeter.ac.uk

20 *Submission to: **Lithos***¹

21
22
23 **Keywords:** Eclogite, base metal sulphide, PGE, Kaapvaal, Roberts Victor, metallogenesis

24
25

¹ **Abbreviations:** base metal sulphide (BMS), platinum-group elements (PGE), electron probe microanalysis (EPMA), scanning electron microscope (SEM), laser ablation inductively coupled plasma mass spectrometry (LA-ICP-MS), working distance (WD), back scattered electron (BSE), energy dispersive spectrometer (EDS)

26 **Abstract**

27 Platinum-group elements (PGE) display a chalcophile behaviour and are largely hosted by base metal
28 sulphide (BMS) minerals in the mantle. During partial melting of the mantle, BMS release their metal
29 budget into the magma generated. The fertility of magma sources is a key component of the
30 mineralisation potential of large igneous provinces (LIP) and the origin of orthomagmatic sulphide
31 deposits hosted in cratonic mafic magmatic systems. Fertility of mantle-derived magma is therefore
32 predicated on our understanding of the abundance of metals, such as the PGE, in the asthenospheric
33 and lithospheric mantle. Estimations of the abundance of chalcophile elements in the upper mantle
34 are based on observations from mantle xenoliths and BMS inclusions in diamonds. Whilst previous
35 assessments exist for the BMS composition and chalcophile element budget of peridotitic mantle,
36 relatively few analyses have been published for eclogitic mantle. Here, we present sulphide
37 petrography and an extensive *in situ* dataset of BMS trace element compositions from Roberts Victor
38 eclogite xenoliths (Kaalpvaal Craton, South Africa). The BMS are dominated by pyrite-chalcopyrite-
39 pentlandite (\pm pyrrhotite) assemblages with S/Se ratios ranging 1200 to 36,840 (with 87% of analyses
40 having S/Se < 10,000). Total PGE abundance in BMS range from 0.17 to 223 ppm. We recognise four
41 end-member compositions (*types i to iv*), distinguished by total PGE abundance and Pt/Pd and Au/Pd
42 ratios. The majority of BMS have low PGE abundances (< 10 ppm) but *Type iv* BMS have the highest
43 concentration of PGE recorded in eclogites so far (> 100 ppm) and are characteristically enriched in
44 Os, Ir, Ru and Rh. Nano- and micron-scale Pd-Pt antimonide, telluride and arsenide platinum-group
45 minerals (PGM) are observed spatially associated with BMS. We suggest that the predominance of
46 pyrite in the xenoliths reflects the process of eclogitisation and that the trace element composition of
47 the eclogite BMS was inherited from oceanic crustal protoliths of the eclogites, introduced into the
48 SCLM via ancient subduction during formation of the Colesberg Magnetic Lineament c. 2.9 Ga and the
49 cratonisation of the Kaapvaal Craton. Crucially, we demonstrate that the PGE budget of eclogitic SCLM
50 may be substantially higher than previously reported, akin to peridotitic compositions, with significant
51 implications for the PGE fertility of cratonic mafic magmatism and metallogenesis. We quantitatively

- 52 assess these implications by modelling the chalcophile geochemistry of an eclogitic melt component
- 53 in parental magmas of the mafic Rustenburg Layered Suite of the Bushveld Complex.

54 **1. Introduction**

55 Platinum-group elements (PGE; Os, Ir, Ru, Rh, Pt, Pd) and most transition metals have an affinity for
56 sulphur (i.e., are chalcophile) and are largely hosted by base metal sulphide (BMS) minerals in the
57 mantle (e.g., Barnes et al., 2015; Lorand & Luguet, 2016; Luguet & Reisberg, 2016 and references
58 therein). During partial melting of the mantle, BMS undergo melting and release their metal budget
59 into the magma generated. Hence if a mantle source region has BMS strongly enriched in PGE or other
60 metals, magma produced by partial melting of that region (particularly a significant degree of partial
61 melting, e.g., > 20%) will also be enriched in these elements and thus will be 'fertile'. However, there
62 are differences in the compatibility and thus mobility of individual PGE and their host minerals, adding
63 complexity to the partial melting regime and correspondingly the concentration of these metals in
64 magma generated. For example, Ir-group PGE (IPGE; Os, Ir and Ru, which behave comparably to Ni
65 and Co) can be hosted by sulphide as well as discrete platinum-group minerals (PGM), spinel-group
66 minerals (e.g., chromite) and even olivine (e.g., Brenan & Andrews, 2001; Ahmed & Arai, 2002; Pitcher
67 et al., 2009; Locmellis et al., 2013). In contrast, most Pt-group PGE (PPGE; Rh, Pt, Pd which broadly
68 behave in a similar geochemical manner to Cu and Au) are largely hosted by sulphides only, although
69 Pt may also be hosted by discrete PGM, either within or on the margins of BMS or sometimes as alloys
70 with other PGE (notably IPGE) (e.g., Lorand et al., 2013; Lorand and Luguet, 2016 and references
71 therein; Gonzalez-Jimenez et al., 2020). Thus the PGE have been subdivided based to their behaviour
72 during partial melting of the mantle and apparent compatibility within silicate and oxide minerals,
73 such that IPGE are 'compatible' and PPGE are 'incompatible'. Further, at the pressures and
74 temperatures at which most mantle partial melting takes place, the sulphide budget of the mantle
75 may occur as two coexisting phases: an Fe-rich monosulphide solid solution (MSS) typically relatively
76 enriched in IPGE, and a comparatively PPGE-enriched Ni-Cu sulphide (e.g., Alard et al., 2000; Bockrath
77 et al., 2004; Lorand et al., 2013 and references therein). Combined, the fertility of a mantle source is
78 a concept fundamental to global 'metallogenesis' (the regional-to-global distribution of metals linked
79 by magmatic and tectonic processes) and likely has further implications for the metallic signature, or

80 'metal basket', of mineralisation linked to mantle-derived (ultra)mafic magmatic systems (e.g., Hughes
81 et al., 2015, 2017).

82 Estimations of the abundance of chalcophile elements in the cratonic subcontinental lithospheric
83 mantle (SCLM, and various regions and lithologies thereof) are based on observations from mantle
84 xenoliths and diamond inclusions (e.g., Bulanova et al., 1996; McDonald et al., 1996; Becker et al.,
85 2006; Aulbach et al., 2012; McDonald et al., 2017). Indeed, mantle xenoliths containing BMS minerals
86 and sulphide inclusions within diamonds provide our only direct insight into the abundance of
87 chalcophile elements at depth. BMS contained within these SCLM-derived samples (whether in
88 xenoliths or as inclusions in diamonds) are commonly divided into two, E-type (eclogitic) and P-type
89 (peridotitic) based on the sulphide composition and associated silicate phase assemblage (e.g., Stachel
90 & Harris, 2008; Kiseeva et al., 2017a). For example, published trace element data from BMS inclusions
91 in diamonds and mantle xenoliths suggest a significant difference in the concentration of chalcophile
92 elements including PGE and other precious and transition metals, between eclogitic and peridotitic
93 mantle (e.g., McDonald et al., 2017).

94 Globally, most published mantle xenolith *in situ* BMS analyses and diamond BMS inclusion data report
95 major element and Re-Os isotopic compositions, and lack information regarding the concentration of
96 PGE and other minor or trace metals (with the notable exceptions of Aulbach et al. (2012) for BMS
97 inclusions in E-type diamonds, and Gréau et al. (2008) and Burness et al. (2020) for cratonic eclogite
98 xenoliths). Other published PGE data for eclogites are bulk rock analyses – such as McDonald & Viljoen
99 (2006) for Orapa eclogite xenoliths and Dale et al. (2009) for ophiolitic eclogites. Eclogite xenolith data
100 from Gréau et al. (2008) and Burness et al. (2020) indicate that the PGE and precious metal budget for
101 this mantle lithology is very low; this is corroborated by the composition of E-type diamond BMS
102 inclusions (e.g., Orapa, Botswana, McDonald et al., 2017; Diavik, Canada, Aulbach et al., 2012) in
103 comparison to the relatively PGE-rich composition of P-type diamond BMS inclusions (Bulanova et al.,
104 1996). In this contribution we present *in situ* analyses of BMS in eclogite xenoliths from the Roberts

105 Victor kimberlite in South Africa and use these data to estimate the precious metal and metalloid
106 budget of the eclogitic SCLM of the Kaapvaal Craton. We examine the range of the eclogitic sulphide-
107 hosted metal budget using the abundant BMS in the Roberts Victor xenoliths and compare these to
108 different mantle source lithologies (e.g., peridotitic) to explore the implications of mantle source
109 characteristics for the fertility of mantle-derived magmas, mineralisation linked to (ultra)mafic
110 magmatic systems and metallogenesis.

111 **1.1 Geological setting**

112 The Kaapvaal Craton of southern African is one of the oldest and thickest sections of crust on Earth
113 (Eriksson et al., 2011). After stabilising c. 3.2-2.8 Ga, it collided with the Zimbabwe Craton becoming
114 sutured by the Limpopo Belt and thus forming the Kalahari Craton (e.g., de Wit et al., 1992; Schmitz
115 et al., 2004; Simon et al., 2007; Brey and Shu, 2018). Largely composed of tonalite-trondhjemite-
116 granodiorite (TTG) suites and Archaean granitic gneisses, the Kaapvaal Craton comprises four crustal
117 blocks: the Kimberley Block (Western Block), the Witwatersrand and Swaziland blocks (Eastern Block),
118 and the Pietersburg Block (e.g., Good and de Wit 1997; Griffin et al., 2003a and references therein) –
119 Figure 1.

120 The Witwatersrand and Kimberley blocks are separated by the Colesberg magnetic lineament, which
121 marks a palaeo-subduction zone between the two blocks that collided c. 2.88 Ga (Schmitz et al., 2004;
122 Brey and Shu, 2018 and references therein) resulting in subduction of c. 2.95 Ga oceanic lithosphere
123 underneath the Western Block (Shu et al., 2013). This process corresponds with a c. 2.9 Ga major
124 metasomatic event in the Kaapvaal Craton, which led to eclogite and eclogite-hosted diamond
125 formation (e.g., Jacob et al., 2003; Richardson et al., 2004) recorded in samples from the Roberts
126 Victor, Jagersfontein, Kimberley and Jwaneng kimberlites. These events also coincide with a peak in
127 Re-Os ages of the Kimberley Block (Schmitz et al., 2004 and references therein) and S-isotopic mass-
128 independent fractionation (S-MIF) is evidence for surficial sulphur having been transferred to the
129 SCLM by this time (e.g., Thomassot et al., 2017).

130 The Kaapvaal Craton has experienced several episodes of kimberlitic intrusions since at least 1.2 Ga,
131 and notably over the last c. 200 Myr, coincident with the break-up of Gondwana ca. 180 Ma (Jelsma
132 et al., 2009). A number of kimberlites, including the 125 Ma Roberts Victor kimberlite pipe, occur on,
133 or proximal to, the Colesberg magnetic lineament (e.g., Schmitz et al., 2004 and Fig. 1). Roberts Victor
134 lies about 40 km east of Boshof on the Kaapvaal Craton (Field et al., 2008). It consists of at least seven
135 different kimberlites, among which are two pipes and two dykes (Gurney and Kirkley, 1996; Field et
136 al., 2008). The kimberlites belong to the micaceous Group II kimberlites and the phlogopite/biotite
137 ages range from 124 to 128 Ma (e.g., Tappe et al., 2018).

138

139 ***1.2 Roberts Victor eclogite xenoliths***

140 For more than 50 years, the eclogite xenoliths of Roberts Victor kimberlite have been extensively
141 studied (e.g., MacGregor and Carter, 1970; Garlick et al., 1971; Manton and Tatsumoto, 1971; Harte
142 and Gurney, 1975; Ozima and Saito, 1975; Hatton and Gurney, 1977; Kramers, 1979; MacGregor and
143 Manton, 1986; Ongley et al., 1987; Sautter and Harte, 1988; Viljoen et al., 1991; Jacob et al., 2003,
144 2005; Huang et al., 2010; Gréau et al., 2013; Kiseeva et al., 2017b; Burness et al., 2020). Early studies
145 recognised that an unusual feature of this pipe is its substantially larger proportion of mafic xenoliths
146 in comparison to ultramafic (~80:20) (Chen, 1971; Macgregor and Carter, 1970), and eclogite xenoliths
147 are up to 80 cm in diameter (Gurney and Kirkley, 1996). Isotopic studies of the eclogite xenoliths led
148 researchers to suggest that their protolith was altered oceanic crust (Ongley et al., 1987),
149 subsequently confirmed by petrological and geochemical studies (e.g. Jacob, 2004).

150 Based on the textural characteristics and major and minor element composition of garnet and
151 clinopyroxene, Macgregor and Carter (1970) identified two types of eclogitic xenoliths in Roberts
152 Victor kimberlites: Texturally, Type I is more altered than Type II, and contains secondary material
153 surrounding every primary grain of garnet or clinopyroxene. This secondary material in Type I xenoliths

154 is compositionally distinguished by high Na₂O (≥ 0.07 wt.%) in garnet and high K₂O (≥ 0.08 wt.%) in
155 clinopyroxene. In Type II eclogites, garnet and clinopyroxene contain ≤ 0.07 wt.% Na₂O and ≤ 0.08
156 wt.% K₂O, respectively. Huang et al. (2012) and Gréau et al. (2011) reported that eclogite xenoliths of
157 both types were sourced from similar depths (170-200 km, using the garnet-clinopyroxene
158 geothermometer of Krogh (1988) and pressure estimates derived from projections of the geotherm),
159 close to the base of the Kaapvaal SCLM. Huang et al. (2012) also expanded their classification,
160 identifying higher concentrations of light rare earth elements (LREE) and large ion lithophile elements
161 (LILE) in Type I xenoliths.

162 Mantle 'metasomatism' evidenced by Roberts Victor eclogites has been investigated: Huang et al.
163 (2014) reported zones of alteration observed within one xenolith and proposed that these may reflect
164 multiple pulses of metasomatism that resulted from interaction in an open system with mantle fluids
165 of varying major and trace element and isotopic compositions. Kiseeva et al. (2017b) investigated a
166 Type I eclogite xenolith and, similarly to the previous studies, reported enrichments in Na, K, Ba, Ti
167 and REE. However, the authors hypothesised that the origin of this metasomatic alteration could be
168 in the incipient melting of the eclogite itself rather than introduction of mantle metasomatic fluids or
169 melts. We ask, what effect would metamorphism, incipient melting, or open system metasomatism
170 have on the BMS composition and chalcophile element budget of these eclogites, and can we
171 distinguish between these processes?

172

173 **2. Methodology and analytical techniques**

174 ***2.1 Samples and petrography***

175 Seven individual diamond-free Roberts Victor eclogite xenoliths, mostly ranging in size from 3 to 5 cm,
176 were used in this study. Detailed silicate textural and chemical analyses are available for the largest of
177 these samples (SS2, sized 20 x 15 x 7 cm) (Kiseeva et al., 2017b). All samples were chosen as

178 representative samples from this pipe and are bimineralic with omphacitic clinopyroxene and pyrope-
179 almandine garnet as the modal minerals and interpreted as primary phases.

180 Petrographic observations were made using reflected and transmitted light microscopy.
181 Photomicrographs of samples except SS2 were captured using a Nikon Eclipse E600 Pol microscope
182 with a 5MP Nikon Digital Sight camera at the Camborne School of Mines (CSM, University of Exeter).
183 Further petrographic examination was carried out using back-scattered electron (BSE) imaging on a
184 JEOL JXA-8200 Superprobe electron probe microanalyser (EPMA, located at CSM) as a scanning
185 electron microscope (SEM) using X-ray Energy Dispersive Spectrometers (EDS) and under high vacuum
186 at 7×10^{-4} Pa. For BSE imaging, the instrument was run with an accelerating voltage of 15 kV or 20 kV
187 with a 1 nA beam current. Searches for platinum-group minerals (PGM) were conducted by energy
188 dispersive x-ray spectrometry (EDS) on a Schottky field emission Hitachi SU-70 field emission SEM at
189 the CSL (Central Science laboratory), University of Tasmania, which is equipped with an Oxford AZTec
190 microanalysis system with X-Max80 SDD EDS detector. Operating conditions were accelerating voltage
191 15 kV, probe current 300–400 pA, and spot size 100–200 nm. BSE imaging of the sample SS2 was
192 conducted using CAMECA SX-5 FE at the University of Oxford. Table 1 provides sample information
193 regarding the texture and location of BMS in the seven eclogite xenoliths.

194 **2.2 QEMSCAN**

195 The mineral assemblage of three polished thin sections (RV-IM-01, RV-IM-15 and RV-IM-18) was
196 analysed using a QEMSCAN® 4300 at CSM, University of Exeter, UK (Gottlieb et al., 2000, Goodall et
197 al., 2005, Goodall and Scales 2007). The software packages iMeasure version 4.2SR1 and iDiscover
198 4.2SR1 and 4.3 (Rollinson et al. 2011) were used for sample measurement and data processing. The
199 samples were carbon coated to 25 nm prior to analysis using an Emitech K950 carbon coater.

200 The QEMSCAN® 4300 system settings were the default of 25 kV, 5 nA, a 1000 X-ray count rate per
201 pixel, a WD of around 22 mm under high vacuum and beam calibration every 30 minutes. The

202 fieldscan measurement mode was used to analyse the samples. For sample RV-IM-01 the whole
203 sample area (18 x 27mm approximately) was measured at an X-ray resolution/pixel spacing of 10
204 microns and a 1500 micron squared field size (x 43 magnification), with two smaller areas scanned at
205 an X-ray resolution/pixel spacing of 1 microns and a 300 micron squared field size (x 224 magnification)
206 for improved detail. The two smaller areas had scan areas of 1 mm² and 2 mm² approximately.

207 For samples RV-IM-15 and RV-IM-18, the fieldscan measurement mode was used to analyse selected
208 small areas at an X-ray resolution/pixel spacing of 1 micron and a 300 micron squared field size (x 238
209 magnification) for improved detail. For sample RV-IM-15 three small areas were measured on the thin
210 section with scan areas of ~1mm², ~2 mm² and ~3 mm². For sample RV-IM-18, two small areas were
211 measured on the thin section, both with scan areas of 1 mm² approximately. The areas were selected
212 to target sulphides and provide high resolution data.

213 Data processing and database development was employed to add and improve SIP (database)
214 categories to match the samples and all of the mineral categories were checked (examination of
215 elemental abundance, elemental ratios, BSE). Specific attention was given to the sulphide minerals
216 such as pyrite, pyrrhotite, chalcopyrite, pentlandite/violarite and sphalerite. The effects of excitation
217 volume were also checked and boundary effect database entries added to handle these. Finally,
218 boundary phase processors were applied to improve edge effects and remove rogue pixels. Data
219 collection and processing followed in-house QC/QA procedures. A summary of QEMSCAN BMS
220 mineral association data are presented in Table 2 and a full list of all mineral association data are
221 available in Supplementary Table A.

222 **2.3 BMS Mineral chemistry**

223 *2.3.1 Electron Probe Microanalysis (EPMA)*

224 Samples were coated with ~25 nm of carbon. Quantitative spot microanalyses of BMS per xenolith
225 were obtained using a JEOL JXA-8200 Superprobe at CSM. Both instruments were each fitted with four

226 WDS detectors, each of which were fitted with two crystals (TAP, LDE, LIF or PET). Analyses at CSM
227 were carried out at a 15 keV accelerating voltage, 14 nA beam current and 10 μm spot size. Counting
228 times for all elements were 20 s for the peak and 10 s for the background. Major elements analysed
229 for sulphides are S, Fe, Ni, Cu and Co. Elements were calibrated prior to analysis with MicroAnalysis
230 Consultants Ltd and Astimex Standards Ltd mineral standards including Astimex pyrite, pentlandite,
231 and metallic standards for Co and Cu. Accuracy was assessed by measuring multiple spot analyses of
232 selected sulphide mineral standards (Astimex pyrite and pentlandite) – see Supplementary Table B.
233 Lower limits of detection (LLD) were calculated using 3σ and are ≤ 0.12 wt.% for S, ≤ 0.15 wt.% for Fe,
234 ≤ 0.17 wt.% for Cu, 0.07 wt.% for Co and 0.14 wt.% for Ni respectively. A summary of EPMA sulphide
235 data are presented in Table 3 and a full list of data are available in Supplementary Table C.

236 *2.3.2 Laser ablation inductively coupled plasma mass spectrometry (LA-ICP-MS)*

237 Time-resolved analysis (TRA) by LA-ICP-MS was performed on each BMS analysed at Cardiff University
238 in two time periods using a UP213 Laser Ablation system coupled initially to a Thermo X Series 2 ICP-
239 MS (RV-IM samples) and later to a Thermo iCAP RQ ICP-MS (SS2 samples). Line analyses were used
240 and all lines were independently calibrated. Where size permitted, sulphides underwent multiple line
241 analyses. A minimum length of ~ 80 μm and a beam diameter of 40 μm were used, with laser operating
242 conditions of 10 Hz frequency, 0.063 mJ at ~ 5 Jcm^{-2} and sample translation at 6 $\mu\text{m sec}^{-1}$. Acquisition
243 times ranged from 50 to 200 seconds with a gas blank measured for 20 seconds prior to laser ablation.
244 Major element abundances (Fe, Ni, Cu, S) of the sulphide were measured by EPMA (section 2.3.1) and
245 a representative ^{33}S per BMS was used as an internal standard for trace element calibration. This was
246 typically 45 wt.% S as a mean of pentlandite, chalcopyrite, rare pyrrhotite, and pyrite, and in line with
247 the mean S concentration of sulphides in eclogitised gabbros (47.5 wt.%) in the Zermatt-Saas ophiolite
248 (Dale et al., 2009). Gas blank subtraction, TRA timeslice selection and internal standard corrections
249 were carried out on Thermo Plasmalab software (RV-IM samples) and Qtegra software (SS2 samples).

250 Five synthetic Ni-Fe-S quenched sulphide standards (numbered 1 to 5) were used for calibration. These
251 included S, Ni, Fe and Cu as major elements and Co, As, Se, Ru, Rh, Pd, Ag, Cd, Sb, Te, Re, Os, Ir, Pt, Au
252 and Bi as trace elements (and on some analytical runs, Mo and Pb). See Prichard et al. (2013) for the
253 compositions and details of analytical methods for these standards and Smith et al. (2014) for further
254 procedural details. Standards 1 to 3 were used for calibration of Fe, Ni, Cu, Co, Zn and Cd and matrix-
255 matched corrections for argide species that interfere with light PGE isotopes ($^{59}\text{Co}^{40}\text{Ar}$, $^{61}\text{Ni}^{40}\text{Ar}$,
256 $^{63}\text{Cu}^{40}\text{Ar}$, $^{65}\text{Cu}^{40}\text{Ar}$ and $^{66}\text{Zn}^{40}\text{Ar}$). Standard 1 (bearing 143 ppm Cd) was also used in corrections for ^{106}Cd
257 on ^{106}Pd and ^{108}Cd on ^{108}Pd . Independent corrections for isotopes of the same element (e.g., $^{66}\text{Zn}^{40}\text{Ar}$
258 and ^{106}Cd on ^{106}Pd , and ^{108}Cd on ^{108}Pd) showed < 20% variance for Ru isotopes at concentrations from
259 0.1-0.2 ppm Ru and 3-10% for Pd isotopes at concentrations around 1 ppm Pd, indicating that the
260 correction criteria are appropriate.

261 Accuracy for PGE and Au was monitored by analysis of the Laflamme-Po724T ('Mem FeS') pyrrhotite
262 standard and the University of Quebec at Chicoutimi (UQAC) FeS1 sulphide standard, as unknowns
263 against the Cardiff quenched sulphide standards (results in Supplementary Table D). Based on these
264 two standards, 1σ precision is typically from 1.6 to 11.2%. A summary of LA-ICP-MS data are presented
265 in Table 4 and a full list of data are available in Supplementary Table E, including argide and isobaric-
266 corrected data with values displayed by isotope (for Ru, Rh and Pd).

267 **3. Results**

268 ***3.1 Sample petrography – QEMSCAN® and microscopy***

269 QEMSCAN® was used to assess the intricate mineralogical and textural relationships within the
270 xenoliths and particularly the BMS. Figure 2a presents a full thin section false colour mineral map of
271 sample RV-IM-01 with higher resolution scans of two BMS in Figures 2b-e. Pyrope and omphacite form
272 up to ~90% of the modal mineralogy (Table 1). These larger 'primary' grains are typically fringed by
273 channels of finer, intergrown (locally spongy) 'secondary' accessory minerals including Na-poor

274 diopside clinopyroxene, albite, K-feldspar, and biotite, with very minor alteration to chlorite and talc
275 (Figure 2 and Supplementary Figure B). Ilmenite and rutile occur as < 1 mm rare accessory grains in
276 some samples.

277 Through a combination of reflected light microscopy, SEM mapping and QEMSCAN® analyses, BMS
278 are found to be dominated by pyrite (Fig. 3c-f, Table 2), with lesser pentlandite, Ni-rich pyrite and
279 chalcopyrite, and rare pyrrhotite (e.g., Fig. 2b-c, 3a-b, Table 2). Pyrite typically bears fine lamellae or
280 net-textured pentlandite, or a Ni-rich pyrite (possibly vaesite and/or violarite or millerite) and rimmed
281 by blocky chalcopyrite. Pentlandite and/or Ni-rich pyrite typically form < 5 to ~45 area % based on
282 visual estimates and confirmed by QEMSCAN® quantitative data for a representative selection of BMS
283 scanned (Table 2). Chalcopyrite is visible in the majority of BMS but is generally a minor phase in most
284 BMS (< 15%, e.g., Table 2) although BMS lacking a significant Fe-sulphide component and only
285 containing pentlandite and chalcopyrite were identified (e.g., Supplementary Figure B(b)). These
286 specimens have a higher apparent chalcopyrite abundance (up to 42 %). However, we note that the
287 *apparent* proportions of end-member sulphide minerals within the BMS grains are dependent upon
288 the level of exposure achieved through polished thin section or polished block production. These are
289 likely to vary significantly depending on whether the exposed 2D surface cross-cuts the centre of a
290 BMS, or its margin.

291 The BMS grains occur in two principal textural settings: (i) predominantly interstitial to the primary
292 silicate minerals along grain boundaries of pyrope and omphacite (e.g., Supplementary Fig. B(d)) and
293 in the channels of finer 'secondary' minerals (e.g., Fig. 2b-c and Supplementary B a-b) and (ii) as
294 inclusions and/or embayments within both these silicates (e.g., Fig. 2d-e and Supplementary Fig. B c
295 and e). Included BMS range in diameter from approximately 70 to 150 µm. They are either rounded
296 or have a polygonal shape. The embayments are locally accompanied by a rim of fine spongy
297 'secondary' clinopyroxene with variable Na content. In contrast, BMS grains interstitial to the 'primary'
298 silicate mineralogy of the xenoliths occur as rounded droplets (Fig. 3a-b) or as highly irregular shapes

299 (Fig. 3c-f) and typically range from 50 to > 500 μm in width, with most > 200 μm . Most interstitial BMS,
300 and some embayments, preserve thin stringers of pyrite intermingled in the channels with 'secondary'
301 silicates, especially clinopyroxene (e.g., Fig. 2d-e, 3e-f). Overall, 79% of BMS observed in this study are
302 interstitial and 21% are included or embayed (Table 5). We observed no systematic difference in the
303 proportion of end-member sulphide minerals (e.g., chalcopyrite, pentlandite, pyrite or pyrrhotite)
304 according to BMS position within the xenolith (included, embayment, or interstitial).

305 **3.2 BMS major element geochemistry (by EPMA)**

306 A summary of the *in situ* major element compositions of BMS from five of the eclogite xenoliths
307 included in this study are presented in Table 3, as measured by EPMA. In Figure 4 we compare the
308 compositions from our study to BMS compositions of eclogite xenoliths at Roberts Victor reported by
309 Gréau et al. (2013), and diamond inclusions at Roberts Victor (and globally) as reported by Deines &
310 Harris (1995). Pyrrhotite, as quantitatively analysed in RV-IM-06 only, has a mean of 40.1 wt.% S and
311 56.8 wt.% Fe with minor Ni (2.43 wt.%). All other Fe-rich end-member sulphides measured were pyritic
312 (52.1-53.2 wt.% or 65.9-66.8 at.% S; Table 3 and Fig. 4a). The precise composition of pentlandite
313 and/or the Ni-rich sulphide end-members in the BMS was difficult to obtain due to the very fine
314 lamellae intergrown with pyrite or pyrrhotite and the relative spot size of the EPMA. Thus, Ni-bearing
315 sulphides in BMS are largely represented by the range of 'Py (\pm Ni)' in Figure 4b and Table 3. The major
316 element compositions of the Fe-Ni-S sulphides in this study directly overlap the range of compositions
317 from Gréau et al. (2013) – Figure 4b. The composition of chalcopyrite documented in our study more
318 closely resemble the end-member composition of chalcopyrite than those recorded by Gréau et al.
319 (2013) – Figure 4c. The concentration of Co is generally low (< 1 wt.%) for all sulphide end-members
320 (Table 3).

321 Using ratios of major elements from our LA-ICP-MS data, we find that most BMS analysed in this study
322 have Ni/(Ni+Cu+Fe) of < 0.3 (Fig. 5a) and this spans a similar range in compositions as determined for
323 E-type (Ni/(Ni+Cu+Fe) < 0.18; Aulbach et al., 2012; McDonald et al., 2017) and P-type BMS inclusions

324 in diamonds ($\text{Ni}/(\text{Ni}+\text{Cu}+\text{Fe})$ 0.02 – 0.68; Bulanova et al., 1996; McDonald et al., 2017). However, all
325 BMS in RV-IM-02 (and some from RV-IM-06 and RV-IM-15) have elevated $\text{Ni}/(\text{Ni}+\text{Cu}+\text{Fe})$ ratios > 0.30 ,
326 more akin to P-type BMS inclusions in diamonds. Most BMS analysed in this study have $\text{Cu}/(\text{Cu}+\text{Ni}+\text{Fe})$
327 ratios equivalent to E-type diamond inclusions (0.005 – 0.30); however, BMS in RV-IM-02 fall at the
328 lower end of this range (0.005-0.05) more similar to the P-type diamond inclusions (Fig. 5b).

329 **3.3 BMS trace element composition**

330 Trace element data from *in situ* LA-ICP-MS analyses of BMS in the Roberts Victor eclogites are
331 summarised in Table 4 and the full data set is provided in Supplementary Table E. A selection of time-
332 resolved analyses (TRA) are presented in Supplementary Figure C.

333 The Roberts Victor eclogite xenolith BMS compositions are compared to BMS compositions in mid-
334 ocean ridge basalts (MORB; Patten et al., 2013), BMS in mid-ocean ridge (MOR) peridotites (Alard et
335 al., 2005), BMS inclusions in olivine from picritic MOR lavas (Savelyev et al., 2019), and BMS inclusions
336 in E- and P-type diamonds (Bulanova et al., 1996; Aulbach et al., 2012; McDonald et al., 2017) in Figures
337 5 to 7. There is a broad correlation between total PGE and major element compositions of BMS (Fig.
338 5), such that higher Ni content BMS have higher total PGE abundances (Fig. 5a). With the exception of
339 RV-IM-02, all samples from this study have low total PGE concentrations ($< 100\text{ppm}$, with most < 10
340 ppm) consistent with the compositional range of BMS inclusions in E-type diamonds. RV-IM-02 BMS
341 are the notable exception, exhibiting compositions more akin to BMS inclusions in P-type diamonds
342 (Fig. 5a-b). The eclogite BMS have a range of Cu concentrations (described by $\text{Cu}/(\text{Cu}+\text{Ni}+\text{Fe})$)
343 equivalent to those shown by MORB and both E-type and P-type diamond inclusions (Fig. 5b). There
344 is no clear correlation between Cu content of BMS and total PGE, but we observe that RV-IM-02 BMS,
345 with the highest total PGE content, has one of the lowest $\text{Cu}/(\text{Cu}+\text{Ni}+\text{Fe})$ ratios – Fig. 5b. There is no
346 correlation between BMS compositions in Figure 5 according to whether the BMS are interstitial or
347 included in garnet or clinopyroxene.

348 Chondrite-normalised Ni-PGE-Au-Re-Cu abundances (normalised after Fischer-Gödde et al., 2010)
349 (Figure 6) show that within each xenolith the BMS loosely follow a single compositional trend. With
350 the exception of RV-IM-02, the BMS mostly contain low total Ir-group PGE (IPGE; Os, Ir, Ru) < chondrite
351 and fractionated PGE patterns such that Pd-group PGE (PPGE; Rh, Pt, Pd) > IPGE (Fig. 6). Further
352 similarities in the plots are noted:

353 (i) *Type i*: RV-IM-01, RV-IM-05, RV-IM-15, and SS2 form a group with a U-shaped pattern for
354 the IPGE and mostly negative Au anomalies and both negative and positive anomalies for
355 Pt.

356 (ii) *Type ii*: RV-IM-03 and RV-IM-06 have this same basic pattern as (i) but extremely low PGE
357 concentrations overall (mostly below detection limit, especially for the IPGE, Rh and Pt)
358 and are relatively enriched in Au (> chondrite and lacking an apparent negative anomaly).

359 (iii) *Type iii*: RV-IM-17 has a similar U-shaped IPGE pattern as (i) but are notably enrichment
360 in Pt and Pd (without these occurring as distinct peaks, unlike RV-IM-01, RV-IM-05, RV-
361 IM-15, and SS2) and a systematic negative anomaly for Au.

362 (iv) *Type iv*: RV-IM-02 compositions are distinct from all other BMS analysed in this study, with
363 elevated IPGE such that the chondrite-normalised multi-element patterns are relatively
364 unfractionated and flat for the PGE, but with notable negative anomalies for Au and Re.

365 *Types i to iii* BMS are similar to the range in compositions shown by BMS inclusions in E-type diamonds
366 and MORB (Fig. 6; Aulbach et al., 2012; Patten et al., 2013; McDonald et al., 2017; Savelyev et al.,
367 2018). We also note that these resemble the compositional range of Gréau et al. (2008), although we
368 cannot quantitatively compare our BMS compositions due to the authors presenting primitive mantle
369 normalised diagrams and no accompanying published values. *Type iv* BMS are more comparable to P-
370 type BMS diamond inclusions and overlap some mid-ocean ridge peridotite compositions (Fig. 6;
371 Bulanova et al., 1996). Despite multiple laser measurements of RV-IM-02, our LA-ICP-MS data sample
372 the only two BMS exposed on the surface of the thin section made from this xenolith and therefore

373 represent a relatively uncommon BMS signature across the eclogite xenolith suite as a whole, although
374 we note that these resemble the IPGE compositions of 'Type I' BMS in Gréau et al. (2008).

375 We provide the mean of BMS composition for eclogites, based on all analyses in this study except from
376 RV-IM-02, in Table 4. We suggest that our *Type i* and *Type iii* BMS compositions (i.e., the majority of
377 our data) are equivalent to the 'Group 2' BMS compositions of Burness et al. (2020) while our *Type ii*
378 BMS are equivalent to Burness et al. (2020) 'Group 1' with notable negative anomalies in Pt. However,
379 our *Type iv* BMS are not recognised by the Burness et al. (2020) study, nor Gréau et al. (2008).

380 There is no discernible difference in PGE systematics between those BMS that are interstitial to the
381 silicates compared to those that are included in garnet or clinopyroxene. There is no systematic
382 difference between PGE, Au or Re abundance for the Cu- or Ni-rich BMS phases (Fig. 6 e.g., RV-IM-01,
383 RV-IM-05, RV-IM-06, RV-IM-15 and RV-IM-17) although we note that the BMS in RV-IM-02 have the
384 highest Ni concentration overall.

385 Distinct positive Pt anomalies in Figure 6 correlate with short-lived Pt peaks in the corresponding
386 time-resolved analysis (TRA) for that analysis (e.g., Supplementary Figure C) caused by inclusion of a
387 nano- or micro-nugget or a Pt-bearing platinum-group mineral (PGM). A similar correlation between
388 peaks in Figure 6 and in TRA is also present for Au and to a lesser extent, Pd. The TRA show several
389 Pd-Sb-Bi and Pt-Pd-Sb-Bi peaks indicating these are present as discrete PGM within the BMS,
390 incorporated into some LA-ICP-MS line analyses. Platinum appears to be predominantly hosted within
391 PGM. Based on the time-resolved spectra of all samples, we note many instances where Pd tracks Ni
392 and/or Cu, and Re, Te and Se largely track Fe and S in the BMS. Arsenic is variable in the TRA, especially
393 in pyrite, and there is no systematic association between As, Pt and Pd. The TRA-based observations
394 are largely consistent with PGM search conducted by SEM (Supplementary Figure E) where rounded
395 to elongate Pd (\pm Pt) antimonides and tellurides (\pm Bi, As), generally up to 1 μ m in diameter and typically
396 occurring at the rim of BMS, have been observed. In some cases, PGM in these samples have been
397 identified as likely to be mertieite ($\text{Pd}_{11}(\text{Sb,As})_4 - \text{Pd}_8(\text{Sb,As})_3$). Platinum (\pm Pd) arsenides and Ni-

398 arsenides (significantly smaller than 1 μm and found within BMS) are also noted within some BMS.
399 One electrum grain ($< 1 \mu\text{m}$) on the rim of the BMS was identified during SEM investigation.

400 Figure 7 shows bivariate trace element variations for BMS in Roberts Victor eclogite xenoliths,
401 analysed by LA-ICP-MS, in comparison to BMS inclusions in E- and P-type diamonds. Distinct
402 decoupling of many elements is apparent (e.g., Figs. 7a,c,e; PGE vs. S/Se, PGE vs. Au, and Te vs. Au)
403 while others show moderate correlations (Fig. 7d; Te vs. Se). Further bivariate diagrams are presented
404 in Supplementary Figure D.

405 The S/Se ratios (Fig. 7a and Supplementary Figure D and Table E) range from 1200 to 36840 with $>50\%$
406 of BMS having S/Se > 5500 . Overall this range is similar to the bulk rock S/Se ratios of Gréau et al.
407 (2013) of 500 to 9924 for Type I eclogites and from 16216 to 24277 for Type II eclogites. The measured
408 S/Se is also generally higher than the primitive mantle S/Se ratio of 3300 (McDonough and Sun, 1995)
409 and range in MORB S/Se (2682 to 4014; Patten et al., 2013), reflecting the dominance of pyrite in the
410 Roberts Victor eclogite BMS assemblage (i.e., addition of S to the BMS assemblage via sulphidation to
411 pyrite). The eclogite xenolith BMS display a similar range in S/Se to both P- and E-type diamond BMS
412 inclusions (1260-22350 and 2540-13580, respectively; Bulanova et al., 1996; Aulbach et al., 2012;
413 McDonald et al., 2017) – Fig. 7a. There is no correlation between S/Se ratio and total PGE abundance
414 for specific xenoliths or the data set as a whole. Copper-rich BMS analyses (*Cu,Fe-(Ni) BMS*) tend to
415 have higher S/Se ratios than Ni- or Fe-Ni-rich BMS analyses (except for RV-IM-06), reflecting their
416 slightly lower Se concentrations – Table 4. The concentration of Se in the eclogite xenolith BMS data
417 set ranges from 10 to 308 ppm and is higher (> 100 ppm) in SS2 and RV-IM-01 and low in RV-IM-17 ($<$
418 50 ppm) – Fig. 7b and Supplementary Table E. There is no correlation between Pd and Se (Fig. 7b) and
419 individual BMS signatures show a range of Pd concentrations (up to 40 ppm) irrespective of Se
420 concentration. This contrasts with the P-type diamond BMS inclusion data set of Bulanova et al. (1996)
421 in which a positive correlation exists between Pd (7 to 50 ppm) and Se (17 to 301 ppm), and the E-
422 type diamond BMS inclusion data that have generally very low Pd concentrations (0.03 to 10 ppm) but

423 a significant range of Se contents (29 to 150 ppm; Aulbach et al., 2012 and McDonald et al., 2017). The
424 range in MORB BMS (84 to 129 ppm Se, 0.04 to 45 ppm Pd; Patten et al., 2013) falls within the range
425 of our BMS data.

426 Concentrations of Au are mostly low (< 0.5 ppm) but some analyses show 0.5 to 1.8 ppm
427 (Supplementary Table E) and there is no apparent correlation between major element composition of
428 BMS and Au content (Table 4). Gold concentration is not correlated with total PGE (Fig. 7c); high Au
429 concentrations occur in BMS with low PGE, and vice versa. MORB BMS (Patten et al., 2013) and E-type
430 diamond BMS inclusions (Aulbach et al., 2012 and McDonald et al., 2017) exhibit similar
431 characteristics. Gold contents of P-type diamond BMS inclusions have not been reported (Bulanova et
432 al., 1996).

433 Tellurium and Se are weakly correlated (Fig. 7d), especially in RV-IM-01, and echoed by P-type
434 diamond BMS inclusions (Bulanova et al., 1996) and MORB BMS (Patten et al., 2013) to some extent.
435 Samples SS2 and RV-IM-05 also show a moderately positive correlation between Te and Se but with
436 significantly less variability of concentrations generally forming a tight cluster. Eclogite xenolith BMS
437 contain up to 63 ppm Te, although > 85% of BMS analyses have < 15 ppm. Tellurium and Au are not
438 correlated (Fig. 7e) and with the exception of RV-IM-01, the Roberts Victor eclogite xenolith BMS are
439 consistent with the range of compositions of MORB BMS (Patten et al., 2013) and BMS included in E-
440 type diamonds (Aulbach et al., 2012 and McDonald et al., 2017).

441 The eclogite xenolith BMS samples analysed in this study have low Os contents, from 0.01 to 0.20
442 ppm, with the exception of RV-IM-02, which hosts BMS with up to 13 ppm Os (Figure 7f, Table 4). The
443 $(\text{Re}/\text{Os})_N$ ratio of our samples covers a wide range from 5.7 to 1357. Once again, RV-IM-02 is the
444 exception, with $(\text{Re}/\text{Os})_N$ ratios < 1 as a result of the higher Os concentrations (> 10x chondrite) in
445 these BMS. Excluding the anomalous RV-IM-02, the Roberts Victor eclogite xenolith BMS compositions
446 are consistent with the Os contents and $(\text{Re}/\text{Os})_N$ of a suite of E-type diamond BMS inclusions from
447 across Southern Africa (including Orapa, McDonald et al., 2017) and Diavik (Aulbach et al., 2012). RV-

448 IM-02 plots closer to P-type diamond BMS inclusion compositions (Simelane, 2004 – note that
449 Bulanova et al. (1996) did not report Re data) and the mid-ocean ridge peridotite BMS compositions
450 of Alard et al. (2005). The MORB BMS compositions of Patten et al. (2013) span a range of $(\text{Re/Os})_N$
451 compositions from 3.2 to 77.5 (Fig. 7f). Based on Figure 7f, the range in $(\text{Re/Os})_N$ appears to be largely
452 controlled by the abundance of Os, rather than Re.

453

454

455 **4. Discussion**

456 ***4.1 Sulphur and the source of eclogitic BMS***

457 All xenoliths, apart from RV-IM-06, are dominated by interstitial BMS of a generally pyritic composition
458 (with variable but low Ni and Cu concentrations – Table 3) with some chalcopyrite around the rim (Fig.
459 3d-f). In contrast, BMS in RV-IM-06 are largely included in silicates (89%, typically within garnet),
460 rounded or with a polygonal shape, and pyrrhotite-dominated (with minor areas of pyritic
461 composition), in comparison to the relatively minor interstitial BMS component of this xenolith which
462 is pyrite-dominated. One BMS in RV-IM-01 was also pyrrhotite-dominated, rounded droplet-like in
463 shape, and although interstitial, situated at the edge of what could be interpreted as an embayment
464 in omphacitic clinopyroxene (Fig. 2a-c and Fig. 3a). Our observations of the dominance of pyrite in the
465 BMS budget are consistent with the findings of Gréau et al. (2008, 2013) and Burness et al. (2020).
466 Dale et al., (2009) studied gabbros and eclogites in the Zermatt-Saas ophiolite terrain and found that
467 pyrrhotite is typically wholly or partially replaced by pyrite in eclogites (having been dominated by
468 pyrrhotite in the gabbros). Dale et al. (2009) found that metamorphism of gabbros (with igneous
469 pyrrhotite + pentlandite + minor chalcopyrite) to gabbroic eclogites (with pyrite, minor chalcopyrite
470 and subsidiary pyrrhotite) coincided with a loss of Ni and Cu, a decrease in the metal/S ratio of
471 sulphides preserved in eclogites, an overall reduction of bulk S concentration by 38%, and a reduction
472 in the modal abundance of sulphides. They interpreted this as being caused by metamorphism from

473 gabbro to eclogite (i.e., 'eclogitisation') and highlighted the range in PGE geochemistry between
474 gabbros, 'transitional gabbros' and gabbroic eclogites as evidence for progressive Pd-loss and Pt-gain
475 throughout 'eclogitisation' (Dale et al., 2009). Notably, the concentration of IPGE appeared to be
476 relatively unaffected during this metamorphism – Dale et al. (2009) interpreted this to reflect an
477 inheritance of these elements from sulphides (and oxides) in the precursor gabbro, and therefore the
478 immobility of IPGE during eclogitisation.

479 Based on petrography and the major element compositions of BMS, Gréau et al. (2013) identified two
480 sulphide assemblages in Type I eclogites from Roberts Victor: pyrrhotite-pentlandite-chalcocopyrite and
481 (Ni)-pyrite-'smythite/violarite'-chalcocopyrite. The latter assemblage was attributed to supergene
482 alteration, via sulphidation of the sulphide 'primary' pyrrhotite-pentlandite-chalcocopyrite (Gréau et al.,
483 2013). However, our observations and data challenge the supergene interpretation of Gréau et al.
484 (2013) based on: the ubiquity of the pyrite-bearing assemblage in all our xenoliths (even as inclusions
485 within garnet and clinopyroxene); the co-existence of pyrite-bearing BMS with other interstitial BMS
486 assemblages of pyrrhotite-pentlandite-chalcocopyrite in the same xenolith; that pyrite- and pyrrhotite-
487 bearing BMS assemblages may occur both interstitial to, and included within, silicates; and that PGE-
488 rich *Type iv* BMS are pyrite-bearing. Given that Dale et al. (2009) demonstrated a transition from a
489 pyrrhotite-dominated BMS assemblage to one that is pyrite-dominated may take place during
490 metamorphism of oceanic crust (protolith) to eclogite during tectonic collision and subduction, we
491 suggest that the prevalence of pyrite in the Roberts Victor xenoliths stems from the process of
492 eclogitisation itself, rather than pyritisation by secondary supergene processes within the kimberlite
493 host to the xenoliths. Our findings therefore also echo those of Evans et al. (2014) who identified $\delta^{34}\text{S}$
494 and cobalt zonation of pyrite and BMS assemblages in orogenic eclogites (Alpine and New Caledonia).
495 Evans et al. (2014) interpreted these sulphide assemblages to have been modified and formed during
496 the protracted history of devolatilisation and heterogeneous fluid flow throughout slab subduction
497 and the earliest stages of exhumation, with remineralisation of the slab precipitating pyrite.

498 In the case of cratonic eclogite xenoliths sourced from the SCLM keel, protolith metamorphism is likely
499 to be only one part of the protracted history of these rocks. Hence, in contrast to Dale et al. (2009)
500 and Evans et al. (2014), we must also consider the role of metasomatism and partial melting within
501 the SCLM in modifying the textures, mineralogy and BMS composition of eclogites: BMS geochemistry
502 is likely to reflect the cumulative effects of some/all of these processes. In this way, we are presented
503 with a similar paradigm to that of Kiseeva et al. (2017b) – that of the ‘chicken or egg’ dilemma of
504 metamorphism and incipient mantle melting vs the involvement of speculative mantle metasomatism
505 as an explanation for the geochemical and mineralogical features recorded in eclogite mantle
506 xenoliths.

507 The generally IPGE-poor, PPGE-rich, Re-rich composition of BMS in this study (with the exception of
508 RV-IM-02 *Type iv*) could be indicative of volatile-rich metasomatism adding Pd, Au, Re, S, as recorded
509 in some peridotite mantle xenoliths (e.g., Alard et al., 2011; Delpech et al., 2012). The interstitial siting
510 of the majority of Roberts Victor eclogite xenolith BMS could therefore favour a metasomatic origin;
511 however the range in PGE systematics (Fig. 6) between our four BMS groupings (*types i to iv*) would
512 therefore indicate that the composition of this metasomatic agent was variable (to account for both
513 PGE-poor and PGE-rich signatures). This seems somewhat implausible when compared to the
514 relatively consistent composition of metasomatic BMS in peridotite xenoliths (on a sample suite-by-
515 suite basis) and the general absence of pyrite in the BMS assemblages of peridotite xenoliths. Notably,
516 none of the BMS from Roberts Victor eclogite xenoliths (including RV-IM-02) show any correlation
517 between total PGE and S/Se or Se. Thus the high S/Se ratio of BMS in eclogite xenoliths (echoed by
518 that of BMS inclusions in E-type diamonds) may represent the increased S abundance in BMS due to
519 the shrinking modal abundances of sulphides during eclogitisation (i.e., Dale et al., 2009; Evans et al.,
520 2014). Hence we suggest that the trace element composition of eclogite xenolith BMS has largely been
521 inherited from the protoliths of those eclogites (i.e., directly from the oceanic crust subducted during
522 formation of the Colesberg Magnetic Lineament c. 2.9 Ga, the subsequent metamorphism of those
523 rocks (similar to processes outlined by Evans et al., 2014), and cratonisation of the Kaapvaal and its

524 SCLM keel; Schmitz et al., 2004; Shu et al., 2013; Brey and Shu, 2018). Accordingly, we suggest that
525 the predominance of pyrite reflects the subduction and eclogitisation process itself (e.g., Dale et al.,
526 2009; Evans et al., 2014) rather than any subsequent metasomatic alteration within the cratonic SCLM
527 at very high f_{S_2} (cf. Burness et al., 2020), a general metasomatic overprint (cf. Gréau et al., 2013) or
528 supergene alteration (cf. Gréau et al., 2013).

529 Our interpretation is consistent with the petrological, compositional, and experimental-based
530 interpretations of Kiseeva et al. (2017b), which suggested that *in situ* melting of eclogites alone could
531 produce the geochemical signature of an enriched melt without the need for an external influence by
532 metasomatic fluids. Given their higher incompatible element abundances and lower solidus
533 temperatures than peridotites, such eclogites are a likely *source* of metasomatic fluids to surrounding
534 peridotites (Kiseeva et al., 2017b). The partial melting signature derived from the eclogite itself (e.g.,
535 Kiseeva et al., 2017b) is preserved as channels of ‘spongy’ diopsidic clinopyroxene. We observed
536 veinlets of pyrite branching off from interstitial BMS within these channels (e.g., Figs. 2d-e and 3d-f)
537 and acknowledge this as evidence for some degree of subsequent alteration and/or mobilisation of
538 the sulphides within these channels. The timing of this mobilisation is unclear – this could record an
539 *in situ* partial melting of the eclogites (e.g., Kiseeva et al., 2017b) or much later remobilisation of BMS
540 from decompression during transportation of the xenoliths to the crust in the Roberts Victor
541 kimberlite. Alternatively, this could indicate localised thin section-scale redistribution of S, possibly
542 from fluid infiltration associated with metamorphism (Evans et al., 2014). Regardless of precise timing,
543 the extent of mobilisation appears to be limited and small scale (thin section-scale) and therefore we
544 suggest that this process had little effect on the metal budget of the eclogite BMS.

545

546 **4.2 Characterising the eclogitic metal budget**

547 Overall, we identify four 'end-member' BMS compositions from the Roberts Victor eclogite xenoliths
548 analysed in this study, based on their Ni-PGE-Au-Re-Cu systematics (Fig. 8):

- 549 • *Type i* – BMS from RV-IM-01, RV-IM-05, RV-IM-15, and SS2 have a wide range in Pt/Pd (0.002
550 to 72, mean 3.8) and variable but generally low Au/Pd (0.001 to 13, mean 0.76).
- 551 • *Type ii* – BMS from RV-IM-03 and RV-IM-06 have very low PGE concentrations overall
552 (particularly Pt), low Pt/Pd (0.01 to 0.91, mean 0.26) and high Au/Pd (0.01 to 20, mean 5.6).
- 553 • *Type iii* – BMS compositions from RM-IM-17, similar to *Type i* with Pt/Pd ranging 0.49 to 1.9
554 (mean 1.2) and low Au/Pd (0.001 to 0.08, mean 0.02).
- 555 • *Type iv* – BMS compositions from RM-IM-02 which are characteristically PGE-enriched,
556 particular for IPGE (with flatter PGE chondrite-normalised patterns), Pt/Pd ranging 1.0 to 39
557 (mean 8.7) and Au/Pd ranging 0.004 to 0.03 (mean 0.01).

558 4.2.1 Eclogitic PGE signatures

559 Of the eight xenoliths analysed in this study, five have low total PGE concentrations (typically < 10
560 ppm) in comparison with P-type BMS inclusions in diamonds (Figs. 5-7) or BMS in peridotite xenoliths
561 (e.g., Lugué and Reisberg, 2016; Lorand and Lugué, 2016 and references therein). Three xenoliths
562 (RV-IM-01, RV-IM-17 and RV-IM-02) have higher total PGE budgets than recognised in previous studies
563 of Roberts Victor eclogites (Gréau et al., 2008; Burness et al., 2020) and are generally more enriched
564 than MORB BMS (Patten et al., 2013) – Fig. 5. Of these, two samples (RV-IM-01 and RV-IM-17) have
565 variable but generally high Pt and Pd concentrations (either recorded within BMS in solid solution or
566 as nano- or micro-nuggets). Furthermore, BMS in RV-IM-02 (*Type iv*) have the highest total PGE
567 concentrations (> 100 ppm) of all the xenoliths analysed and are some of the most enriched in eclogite
568 xenoliths recorded so far globally; their IPGE/PPGE ratios and the overall shape of their chondrite
569 normalised multi-element pattern are more akin to P-type diamond inclusions and mid-ocean ridge
570 peridotites (Figs. 5-7 cf. Bulanova et al., 1996; Alard et al., 2005). These findings have significant
571 implications for the PGE budget of the eclogitic SCLM.

572 *Type iv* BMS also resemble ‘Group B’ BMS in lherzolite xenoliths from the marginal cratonic setting of
573 Loch Roag (Scottish Outer Hebrides; Hughes et al., 2017); both have relatively high Ni concentrations
574 ($\text{Ni}/(\text{Ni}+\text{Cu}+\text{Fe}) > 0.3$) and we suggest that this is fundamental to their high total PGE abundance ($>$
575 100 ppm) and high IPGE (Fig. 6). However, we find it unlikely that *Type iv* BMS are directly derived
576 from P-type mantle themselves (cf. Aulbach et al., 2009) not least because *Type iv* BMS appear to be
577 comprised of pentlandite and Ni-pyrite. The BMS in RV-IM-02 are 200-400 μm in diameter, irregular
578 in shape (similar to the shapes of BMS in Fig. 3c-f), interstitial to silicates, and found in channels of
579 spongy diopsidic clinopyroxene (similar to those imaged in Fig. 2b). Hence *Type iv* BMS look similar to
580 any other interstitial BMS observed in the Roberts Victor eclogite xenolith suite (although no
581 significant chalcopyrite component was identified during petrographic inspection of this type of BMS),
582 and would likely be classed as ‘metasomatic’ in origin according to similar textures in peridotite
583 xenoliths (e.g., Aulbach et al., 2016; Lorand and Luguët, 2016).

584 Unlike BMS in peridotite xenoliths, for all of the eclogite xenolith BMS in this study (excluding *Type iv*),
585 we found no systematic differences between PGE or metalloid abundances (specifically Se and Te) vs.
586 the major element composition of each BMS analysis (Ni, Cu or Fe dominance). Thus, the eclogite BMS
587 budget differs significantly from peridotite BMS systematics (e.g., Lorand and Luguët, 2016 and Luguët
588 and Reisberg, 2016 and references therein) in that the BMS trace element compositions appear to be
589 more variable in eclogites. In particular, our data highlight that IPGE concentrations in eclogite xenolith
590 BMS are not uniformly low (e.g., up to 77 ppm in *Type iv* BMS) and that the total PGE (up to 223 ppm
591 in BMS) and PPGE (up to 167 ppm in BMS) budgets of eclogites may be higher than previously
592 reported.

593 4.2.2 *The presence of platinum-group minerals (PGM)*

594 We observe nano- and micron-scale PGM (typically $\leq 1 \mu\text{m}$ diameter) in the eclogite xenoliths,
595 including Pd-Pt antimonides, tellurides and arsenides spatially associated with BMS (Supplementary
596 Figure E). No IPGE-bearing PGM (e.g., Os-Ir alloys) were observed in our samples. The presence of

597 PPGE-bearing PGM (\pm Au) is corroborated by short-lived spikes for Pt, Pd and Au in TRA of LA-ICP-MS
598 data (e.g., Supplementary Figure C). These LA-ICP-MS-based signals are integrated across the length
599 of the laser line and each analysis may accommodate significant fluctuations in Pt (and Pd and Au),
600 introducing an important nugget effect in the *in situ* BMS compositions. Conversely, significant
601 negative anomalies in these elements on normalised plots (Fig. 6) reflect sample volumes where
602 nano/micro-grains have not been intersected by the laser analysis, but nonetheless exist elsewhere
603 within the BMS.

604 To our knowledge, the PGM we describe here are some of the first described occurrences in eclogite
605 xenoliths and we herewith consider their genesis. In peridotite xenoliths, PGM tellurides and
606 bismuthotellurides may be indicative of refertilisation (Eggler and Lorand, 1993; Lorand et al., 2010;
607 Lorand and Luguét, 2016). Alternatively, PGM (such as the rounded to 'blocky' antimonides at the rim
608 of BMS observed in our samples) may be interpreted as forming either by exsolution from a sulphide
609 liquid before MSS and ISS formation (e.g., Peregoedova and Ohnenstetter, 2002; Sinyakova et al.,
610 2016; Helmy and Botcharnikov, 2020; Anenburg and Mavrogenes, 2020) or after sub-solidus
611 transformation (e.g., Fleet et al., 1993; Peregoedova, 1998; Holwell and McDonald, 2010). Kamenetsky
612 and Zelenski (2020) also highlighted a mechanism whereby PGM may form via desulphidation of BMS
613 during fluctuations in the environment of a magmatic plumbing system (e.g., changes in pressure,
614 temperature and chemistry – FeO, fO_2 , fS_2).

615 In contrast, the Pt,Pd-arsenide PGM (typically $< 1\mu\text{m}$ and both rounded and irregular in shape) may
616 be interpreted to represent secondary mineral phases related to localised extraction from BMS at low
617 (non-magmatic) temperatures (e.g., Barkov and Fleet, 2004; Savelyev et al., 2018); thus the presence
618 of PGM-arsenides may support the interpretation of supergene alteration in forming Ni-rich pyrite in
619 eclogite xenoliths (Gréau et al., 2013). However, Gonzalez-Jimenez et al. (2020) highlighted that Pt-
620 arsenides in SCLM-derived peridotite xenoliths may form directly as nanograins in BMS and therefore
621 reflect PGM within the SCLM itself. Alard et al. (2011) and Delpéch et al. (2012) further suggested a

622 link between Pt,Pd-arsenides, tellurides, and bismuthinides in Kerguelen and Montferrier peridotite
623 xenoliths as forming from carbonate and phosphate-related mantle metasomatism. Whilst the precise
624 timing of PGM formation in the Roberts Victor eclogites may not be answered definitively for now,
625 the presence of PGM points to alternative mechanisms by which PGE and the precious metal budget
626 of eclogitic SCLM may become mobilised during partial melting, metasomatism and major magmatic
627 events impinging upon the cratonic keel.

628 *4.2.3 Tellurium, selenium and gold*

629 Tellurium and Se were detected in all eclogite BMS analysed in this study, but generally occur at low
630 concentrations (typically Te < 15 ppm and Se < 150 ppm). This is similar to Te and Se concentrations
631 in BMS inclusions in E-type diamonds (Aulbach et al., 2012; McDonald et al., 2017) and many BMS
632 compositions in peridotite xenoliths (< 10 ppm Te, e.g., Lorand and Alard, 2010). Although Te and Se
633 are generally thought of as coupled chalcophile metalloids in mantle petrology, their chemical
634 behaviour is typically decoupled due to the heterogeneous presence of nano/micro-scale tellurides
635 (e.g., Lorand and Alard, 2010; König et al., 2012; Brenan, 2015; Harvey et al., 2015; Luguët et al., 2015).
636 However, we see a broad correlation between Te and Se in BMS on a sample-by-sample basis for some
637 of the eclogite xenoliths analysed in this study (Fig. 7d – e.g., RV-IM-01, SS2, RV-IM-02), and together
638 with evidence of coupled behaviour in TRA (e.g., Supplementary Figure C for RV-IM-01) we suggests
639 this reflects incorporation of both of these elements in solid solution within BMS, in addition to
640 nano/micro-scale Te-bearing PGM. There is no correlation between Te and Au (Fig. 7e) and this
641 corroborates with an absence of Au-telluride nano/micro-grains associated with BMS in our eclogite
642 xenoliths. The apparently low Au concentrations in BMS may indicate Au decoupling from the sulphide
643 budget with ‘missing’ Au budget accommodated by a non-sulphide mineral phases hosted within
644 silicates, similar to the nano-inclusions of Au found in the strained (deformed and recrystallized)
645 crystal margins of olivine in Pyrenean lherzolites (Ferrais and Lorand, 2014), thus introducing a nugget
646 effect in the sampling. The presence of a Au-bearing nano/micro-mineral phase hosting the ‘missing’

647 Au budget is supported by our finding a rounded grain of electrum (Au,Ag) in association with Ni-pyrite
648 observed in our eclogite samples.

649 The concentration of Pd and Se in BMS inclusions in P-type diamonds (Bulanova et al., 1996) and some
650 bulk rock compositions of peridotite xenoliths (e.g., Harvey et al., 2015) are positively correlated,
651 suggesting similar chalcophile behaviour of the two elements such that Se concentration may be used
652 as a proxy for total PGE abundance. Hence, PGE-rich samples would be expected to have lower mantle-
653 like S/Se ratios (primitive mantle S/Se = 3300 (McDonough and Sun, 1995) vs. 3000 in Pyrenean
654 peridotites (Lorand & Alard, 2010) and chondrite S/Se = 2500 ± 150 (Dreibus et al., 1995)). The
655 concentration of Se in BMS analysed in this study (10 to 308 ppm) overlaps with the composition of
656 peridotitic BMS and MORB BMS (Patten et al., 2013) but have a much wider range in Se abundance
657 (up to 308 ppm). This is similar to the range in Se abundances reported by Burness et al. (2020) in
658 Roberts Victor and Jagersfontein eclogites (49 to 588 ppm) and could reflect the generally lower Ni
659 and S-rich composition (typically pyritic) of the eclogitic BMS in this study (Fig. 5a), in comparison to a
660 mean of 133 ppm in pentlandite, 136 ppm in chalcopyrite and 26 ppm Se in pyrite from Pyrenean
661 peridotites (Lorand and Alard, 2010).

662 Using bulk geochemistry, some mantle xenolith studies have demonstrated that Se may be mobilised
663 during supergene alteration (e.g., Gréau et al., 2013; Harvey et al., 2015). However, *in situ* BMS
664 analysis of a 'pristine' eclogite xenolith by Gréau (2011) has shown that the primary eclogitic S/Se ratio
665 may be superchondritic (6000-10,000), similar to metasomatic peridotite-hosted BMS (e.g., Lorand et
666 al., 2003; Alard et al., 2011) and distinct from sulphides in kimberlites (> 90,000) – Gréau et al. (2013).
667 Given that 87% of our BMS analyses have S/Se ratio < 10,000, we therefore suggest that the trace
668 element signature of eclogitic BMS is still largely representative of their metal budget when *in situ* in
669 the Kaapvaal SCLM, despite alteration to the pyritic assemblages now prevalent in the xenoliths.

670

671 **4.3 Implications for metallogenesis and the metal budget of mantle-derived mafic magmatic**
672 **systems**

673 Models for the source of chalcophile metals in mineralisation linked to mafic magmatic systems
674 typically refer to peridotite partial melting in which BMS in the mantle source are interstitial to the
675 silicate minerals and are assumed to be homogenous in composition (Naldrett (2011)). During partial
676 melting, the most fusible minerals in the source melt first (e.g., BMS, clinopyroxene and garnet) and
677 as partial melting continues, more BMS are incorporated into the silicate melt until the BMS budget
678 of the residue is depleted. Given the strongly chalcophile behaviour of the PGE, and their extremely
679 high partition coefficients between sulphide minerals and silicate melt (e.g., from 4×10^5 (Ru) to $2-3 \times$
680 10^6 (Ir, Pt); Mungall and Brenan, 2014) any BMS left in the mantle source will suppress the uptake of
681 PGE into the silicate melt. However, once partial melting exhausts the BMS budget of the source, the
682 full PGE budget is transferred into the melt. This paradigm is the basis for models describing the
683 fertility of mantle-derived magmas that feed mineralising systems and thus ore deposit models
684 (Naldrett, 2011), although the significance of an incongruent melting scenario has more recently
685 gained momentum (e.g., Holwell et al., 2019; Choi et al., 2020). However, different populations of
686 BMS exist in the mantle and that their various textural settings (interstitial vs included, what silicate
687 mineral assemblage they are associated with, peridotitic vs eclogitic source lithology for partial
688 melting in the mantle, etc) mean that BMS (and the PGE budget thereof) may be unevenly vulnerable
689 to partial melting. For example, given the substantially lower solidus temperatures for eclogites in
690 comparison to peridotites (Yaxley and Brey, 2004; Spandler et al., 2008; Green et al., 2010; Herzberg
691 and Zhang, 1996), eclogite is more likely to undergo extensive partial melting during large magmatic
692 events and therefore eclogite-hosted BMS and its metal budget may be particularly susceptible to
693 mobilisation. Indeed, it is plausible that sulphide may even be physically entrained as droplets within
694 melts derived from such extensive eclogitic partial melting.

695 **4.3.1 An eclogitic source component in parental magmas of the Bushveld Complex?**

696 Southern Africa records several major large igneous provinces (LIP) throughout its history and the c.
697 2.05 Ga Bushveld LIP (Zeh et al., 2015) in particular hosts many of the world's most important
698 orthomagmatic PGE-Ni-Cu ore deposits (e.g., Naldrett, 2011). The source(s) of magmas that fed the
699 Bushveld magmatic event and the controls on the metallogenic signature of this LIP remain debated.
700 Several models now evoke extensive plume-related partial melting of the mantle (Hatton, 1995), with
701 varying proportions of SCLM-derived magmas vs crustal contamination to explain geochemical facets
702 of igneous rocks of the Bushveld LIP (e.g., Harris et al., 2005; Barnes et al., 2010; Zirakparvar et al.,
703 2014, 2019; Zeh et al., 2015, 2020; Wilson et al., 2017). Bushveld-aged diamond-hosted BMS
704 discovered at Venetia and Premier (Richardson & Shirey, 2008) demonstrate a link between LIP events
705 and the formation of some generations of diamonds and mantle BMS. Although contentious, based
706 on Re-Os isotopic evidence from diamond BMS inclusions (Richardson & Shirey, 2008) and Sr-isotopic
707 evidence from quenched ultramafic units in the Bushveld Complex itself (Wilson et al., 2017) some
708 authors have linked the formation of the Bushveld Complex to varying components of partial melting
709 of eclogitic rocks in the SCLM underlying the Complex (e.g., Richardson & Shirey, 2008; Zeh et al.,
710 2015). Richardson & Shirey (2008) put forward a model whereby parental Bushveld magmas were
711 derived from approximately 40% SCLM melting with a 10% eclogitic component for the more
712 magnesian Lower Zone (i.e., a total of 4% eclogitic component to the parental magma), to 75% SCLM
713 melting with 70% eclogitic component for the more aluminous character of the Main Zone. On the
714 face of it, such a significant eclogitic signature in these parental Bushveld magma models (i.e.,
715 Richardson & Shirey, 2008; Zeh et al., 2015) appear to conflict with the average proportion of eclogitic
716 rocks in the cratonic lithosphere which is generally agreed at 1 to 4 % by volume (Schulze, 1989;
717 McLean et al., 2007), consistent with seismic evidence ruling out large clusters of eclogite material in
718 the Kaapvaal SCLM (James et al., 2004). Yet, despite this, eclogitic xenoliths and inclusions in diamonds
719 are disproportionately abundant entrained in some kimberlite-derived magmas.

720 Until recently, due to the lack of data on the PGE abundances in cratonic eclogites available in
721 published literature, it was not possible to quantitatively assess if the PGE budget of eclogitic BMS

722 could contribute significantly to the metal basket of mafic magmatic systems and PGE-enriched
723 intrusions, such as the layered mafic portion of the Bushveld LIP (Rustenburg Layered Suite; RLS). We
724 address this by using the measured BMS compositions in our Roberts Victor eclogite xenoliths to
725 model the chalcophile element budget of magmas produced by partial melting of an eclogitic source
726 in the SCLM. We compare this to the parental magma compositions hypothesised to have fed the
727 layered mafic RLS of the Bushveld in order to comment on the viability of the aforementioned models
728 (e.g., Richardson and Shirey, 2008) from a metallogenic perspective.

729 We modelled the chalcophile (Ni, PGE, Au, Cu) and Re element composition of silicate melts derived
730 from partial melting of Roberts Victor eclogite BMS (as measured in this study) – see Figures 9 and 10
731 and Supplementary Figure F. The details of the modelling method, including partition coefficients and
732 starting compositions, are provided in the Supplementary Information. In each case, we compare the
733 modelled composition of eclogite-derived silicate melt to the composition of the parental magmas of
734 the RLS. The RLS parental magmas compositions are based on quenched contact rocks (including some
735 sills) from the margins of the Lower and lower Critical zones (B1: tholeiitic basalt with Mg# 71), upper
736 Critical Zone (B2: tholeiitic basalt with Mg# 55), and Main Zone (B3: tholeiitic basalt with Mg# 62) –
737 see Barnes et al. (2010).

738 We assume that prior to melting, BMS present in the eclogites would likely be solid, based on P-T
739 estimates of 1150°C and 5-6 GPa for sample SS2 (Kiseeva et al., 2017b) and in line with estimates of
740 other Roberts Victor xenoliths being derived from > 140 km (e.g., Burness et al., 2020) and thus
741 pressures > 3 GPa, with a geothermal gradient of approximately 45 mWm⁻² (Miller et al., 2016). If the
742 eclogite contains carbon (which is likely given their oceanic crust origin), then the sulphide solidus at
743 3 GPa is approximately 1125°C, and 1250°C at 5-6 GPa (Zhang et al., 2015). Accordingly, we modelled
744 the behaviour of chalcophile elements as partitioning between only two phases: 'sulphide' and a liquid
745 silicate melt. Given the strong chalcophile behaviour of the PGE, as reflected by their extremely high
746 Nernst partition coefficients (Mungall and Brenan, 2014), essentially all of the BMS in the source (>

747 99%) must be melted and incorporated into the silicate partial melt in order for it to have any tenable
748 PGE budget (see Supplementary Figure F); thereafter all modelling assumed that 100% of the BMS was
749 melted out of the mantle source and added to the silicate magma formed (Figs. 9-10). This is especially
750 feasible in the case of an eclogitic source where, although the sulphide would be expected to melt
751 before the silicates (Zhang et al., 2015), the silicates themselves are highly fusible.

752 By modelling partial melting of an eclogite source with each of the four end-member BMS
753 compositions in this study, we produced silicate melts of distinct compositions (Figure 9a). Notably,
754 melts derived from a *Type iv* eclogite source (i.e., with BMS of RV-IM-02 composition) are over
755 endowed for all PGE in comparison to all Bushveld parental magmas. Similarly, melts solely derived
756 from a *Type iii* eclogite source are relatively Pt and Pd enriched. Melts derived from a *Type ii* eclogite
757 source (i.e., with BMS of RV-IM-03 and RV-IM-06 composition) are depleted relative to the Bushveld
758 parental magmas, especially for Pt. However, melts derived from a *Type i* eclogite source, and indeed
759 those derived from a mean composition for Roberts Victor BMS (calculated based on all BMS analyses
760 in this study, excluding the rare PGE-enriched RV-IM-02 BMS) produce melts with chalcophile
761 abundances similar to the composition of Bushveld parental magmas B1, B2 and B3. In Figure 9b, we
762 mix *Type i* and *Type iv* BMS in various proportions and demonstrate that the PGE-rich composition of
763 *Type iv* (RV-IM-02) is capable of significantly enriching the total PGE content of a silicate magma
764 produced during partial melting, even if only present in very small proportions (e.g., 5% *Type iv* in the
765 total BMS budget).

766 The variation in eclogite BMS compositions relative to Bushveld parental magmas is further
767 demonstrated in Figure 10. Partial melts derived from an eclogite source with complete BMS melting
768 span the range of total PGE concentrations of the Bushveld parental magmas (Fig. 10a), including the
769 B2 upper Critical Zone composition that is suggested to be fundamental to the metal budget of the
770 main mineralised reefs of the RLS, including the UG2, Merensky Reef, Bastard Reef and Platreef.
771 Furthermore, the Pt/Pd and Ni/Cu ratios of these eclogite-derived melts are close to those found in

772 the Bushveld parental magmas (Fig. 10a-b). It has been suggested that the observed radiogenic Os
773 signatures of the Bushveld reefs were derived directly from the an eclogitic component in the SCLM,
774 on the basis of the high initial $^{187}\text{Os}/^{188}\text{Os}$ of BMS included within 2.05 Ga diamonds (Richardson &
775 Shirey, 2008) and their similarity to the Os-isotopic compositions of PGM and chromitites in the upper
776 Critical Zone of the RLS in the Bushveld – i.e., the stratigraphic point in this layered intrusion where
777 the main PGE-mineralised reefs occur ($^{187}\text{Os}/^{188}\text{Os}$ ranging 0.11 to 0.19 – Hart and Kinloch, 1989;
778 McCandless and Ruiz, 1991; Schoenberg et al., 1999; Coggon et al., 2012). At the time of writing, there
779 is no published Re data for the Bushveld parental magmas (B1-3 and UM), hence we cannot make a
780 direct comparison between our eclogite-derived model melts and Re/Os of the Bushveld magmas.
781 However, comparison to the estimated ‘Bushveld primary melt’ of McCandless & Ruiz (1991) (Re/Os
782 = 28) again demonstrate that the range of eclogitic compositions also reasonably covers this overall
783 Bushveld signature (Fig. 10c).

784 In summary, our chalcophile element models demonstrate that partial melting of SCLM eclogites may
785 be capable of enhancing the metal basket of the asthenosphere-derived parental magmas of the
786 Bushveld LIP. In this sense, SCLM eclogite-derived partial melts may be as PGE-fertile as
787 asthenospheric peridotite-derived melts as a consequence of the variable IPGE-rich and PPGE-rich
788 BMS populations that eclogites contain and the fusible nature of this rock type. Thus, an eclogitic
789 component to the Bushveld parental magmas is supported both isotopically (Richardson & Shirey,
790 2008; Zirakparvar et al., 2014, 2019; Zeh et al., 2015, 2020) and metallogenically (this study).

791

792 **5. Conclusions**

793 1. The BMS are dominated by assemblages bearing pyrite (with variable Ni and Cu content),
794 although some pyrrhotite-bearing BMS are also observed. We interpret the dominance of
795 pyrite to reflect metamorphism of the original pyrrhotite-dominated igneous assemblage of

796 the protolith to the eclogites (in line with interpretations of Dale et al. 2009). Accordingly, the
797 BMS budget was introduced into the SCLM via ancient subduction (i.e., oceanic crust
798 subducted during formation of the Colesberg Magnetic Lineament c. 2.9 Ga and the
799 cratonisation of the Kaapvaal and its SCLM keel; Schmitz et al., 2004; Shu et al., 2013; Brey
800 and Shu, 2018). Whilst some subsequent modification of BMS may have occurred (e.g., Gréau
801 et al., 2013) we highlight that the predominance of pyrite reflects the eclogitisation process
802 itself rather than metasomatic alteration at high f_{S_2} (cf. Burness et al., 2020).

803 2. S/Se ratios of the majority of BMS are < 10,000, in line with the superchondritic S/Se (6000 to
804 10,000) of 'pristine' eclogite xenoliths by Gréau (2011). Hence, the trace element signature of
805 eclogitic BMS is largely representative of their metal budget when *in situ* in the Kaapvaal SCLM
806 keel and we suggest that the trace element composition of eclogite xenolith BMS has chiefly
807 been inherited from the oceanic crustal protoliths of the eclogites.

808 3. We recognise four 'end-member' compositions (*types i to iv*) in the Roberts Victor eclogite
809 xenoliths, distinguished by total PGE abundance and Pt/Pd and Au/Pd ratios. Whilst the
810 majority of these have low total PGE concentrations (typically < 10 ppm), *Type iv* BMS are
811 highly enriched in PGE (> 100 ppm total PGE). Crucially, *Type iv* BMS have the highest recorded
812 PGE abundances in eclogite so far, with a distinctive IPGE-enriched composition and thus
813 indicate that the PGE budget of the eclogitic SCLM may be substantially higher than previously
814 reported.

815 4. We observe PGM in the Roberts Victor eclogite xenoliths, including nano- and micron-scale
816 Pd-Pt antimonides, tellurides and arsenides spatially associated with BMS. To our knowledge,
817 these are some of the first PGM documented in eclogite mantle xenoliths. The PGM may have
818 exsolved from BMS during cooling, however these may also be formed during modification of
819 the BMS (pyritisation).

820 5. Based on isotopic evidence from diamond inclusions and the Rustenburg Layered Suite,
821 authors have previously proposed that partial melting of eclogites in the SCLM have directly

822 contributed to the Bushveld parental magmas (e.g., Richardson & Shirey, 2008; Zeh et al.,
823 2015). However, until recently it was not possible to quantitatively assess if the PGE budget
824 of eclogitic SCLM could contribute significantly to the metal basket of mafic magmatic systems
825 and PGE-enriched intrusions. We modelled the chalcophile (Ni, PGE, Au, Cu) and Re element
826 composition of silicate melts derived from partial melting of Roberts Victor eclogite BMS.
827 Using the mean of *Type I, ii, and iii* BMS compositions, we demonstrate that incorporation of
828 SCLM eclogites (via partial melting) into ascending asthenosphere-derived magma is not
829 detrimental to the metallogenic budget of that magma. Crucially, by incorporating just 5% of
830 *Type iv* BMS into our total eclogitic BMS budget, we find that eclogitic SCLM-derived partial
831 melting could in fact enhance the metal basket of ascending asthenosphere-derived partial
832 melts.

833 **Acknowledgements**

834 *Steve Pendray and Joe Pickles are thanked for sample preparation and lab support, respectively. The*
835 *research in Oxford University was financially supported by NERC grant NE/L010828/1 to ESK. VSK*
836 *acknowledges funding by the Russian Science Foundation grant no. 16-17-10145. IMcD acknowledges*
837 *support from the Natural Environmental Research Council (NERC) under tellurium and selenium cycling*
838 *and supply grant NE/M010848/1. The authors thank Marek Locmellis, Marco Fiorentini and Steve*
839 *Barnes for their constructive and thorough reviews, and José Maria Gonzalez-Jiménez for his editorial*
840 *handling of the paper.*

841 **Figure captions**

842 **Figure 1** – Map of southern Africa showing location of Roberts Victor (RV) kimberlite relative to the
843 Kaapvaal and Zimbabwe cratons and adjoining orogenic belts, the Colesberg Magnetic Lineament, a
844 selection of other kimberlite localities, the Transvaal Supergroup, the Bushveld Complex and the
845 Molopo Farms Complex in Botswana (of the same age as the Bushveld Complex, part of the same
846 Large Igneous Province). Acronyms include Pietersberg block (PB), Kimberley block (KB),
847 Witwatersrand block (WB), Swaziland block (SB). The double line in the West delineates the edge of
848 the Kalahari Craton (consisting Kaapvaal Craton, Zimbabwe Craton, Limpopo Belt and the Kheis – Okwa
849 – Magondi Belt).

850 **Figure 2** – QEMSCAN® false colour mineral maps of RV-IM-01 using field scan technique (see
851 Methods). (a) Whole section scan (at 10 µm resolution) showing relationships between garnet and
852 clinopyroxene (Na-rich, omphacite) with network of ‘spongy’ Na-poor clinopyroxene (labelled ‘Ca Ma
853 (Fe Al) silicates), albite, K-feldspar, biotite and minor chlorite. A grain of phlogopite (± chlorite) is seen
854 on the margin of the xenolith. (b) A 1 µm resolution field scan of a rounded BMS (with chalcopyrite
855 rim and intergrown lamellae of pyrrhotite and pentlandite with minor pyrite) sited within a channel
856 of ‘spongy’ and intergrown Na-poor and Na-rich clinopyroxene with albite at the margin of two Na-
857 rich (omphacite) clinopyroxene crystals. (c) Same area as (b) but highlighting the texture of the BMS
858 and albite in the channel. (d) A 1 µm resolution field scan of a blocky BMS grain at the margin of a
859 garnet and Na-rich clinopyroxene. Notice the Na-poor clinopyroxene (labelled Ca Ma (Fe Al) silicates)
860 along fractures and channels into the Na-rich clinopyroxene. (e) Same area as (d) but highlighting the
861 texture of the BMS and its relationship with pyrite and sphalerite intergrown in the channels with K-
862 feldspar and Na-poor clinopyroxene.

863 **Figure 3** – Reflected light photomicrograph and BSE images of BMS from the Roberts Victor eclogite
864 xenoliths. (a) Reflected light photomicrograph of rounded BMS in RV-IM-01 in a channel of ‘spongy’
865 Na-poor clinopyroxene intergrown with minor K-feldspar at the crystal boundary of primary Na-rich

866 clinopyroxene (omphacite). This is the same area as pictured in Fig. 2(b-c) and comprises pyrrhotite
867 with lamellae of pentlandite and a rim of chalcopyrite. Pock-marks on the surface are the result of
868 polishing and slight tarnishing. (b) BSE image of three rounded BMS in SS2. The BMS towards the top
869 of the image is an embayment in Na-rich clinopyroxene surrounded by a ring of 'spongy' Na-poor
870 diopsidic clinopyroxene (labelled 'Di'). The other two BMS in this image are interstitial, surrounded by
871 channels of spongy 'secondary' accessory minerals. A rounded inclusion of garnet (Grt) is present
872 within the main primary Na-rich clinopyroxene (CPX). (c) BSE image of blocky BMS from RV-IM-06
873 composed entirely of lamellae of pyrite and Ni-rich pyrite (appear striated in image, labelled as mss).
874 Blocky Ni-rich pyrite occur around the rim . The BMS is interstitial to garnet. (d) BSE image of irregularly
875 shaped BMS in RV-IM-15 interstitial to garnet and Na-rich clinopyroxene (and within a channel of
876 intergrown Na-poor clinopyroxene, K-feldspar and biotite). The BMS is partially oxidised (labelled 'ox')
877 and largely composed of lamellae of pyrite and Ni-rich pyrite (labelled mss). Chalcopyrite occurs at the
878 rim through the centre of the grain. (e) Elongate BMS in SS2 similar to (d) and situated as an
879 embayment in Na-rich clinopyroxene with a channel of intergrown Na-poor clinopyroxene and K-
880 feldspar (on the right of the BMS and embayment). Notice that pyrite has become intergrown with
881 silicates in the channel. (f) Bleb-like BMS in SS2 interstitial to garnet and Na-rich clinopyroxene with a
882 nearby channel of Na-poor pyroxene. Pyrite and chalcopyrite have mobilised along these channels
883 forming thin stringers off the rim of the main BMS grain. The BMS grain has the same characteristics
884 as the other BMS presented here (lamellae of pyrite and Ni-rich pyrite (labelled 'mss') with
885 chalcopyrite around the margins and in some lines in the grain). Abbreviations are chalcopyrite (Cp),
886 pyrite + Ni-rich pyrite (mss), Na-rich clinopyroxene (CPX), Na-poor clinopyroxene (Di), garnet (Grt),
887 partial oxidation of sulphides (ox).

888 **Figure 4** – Major element chemistry of BMS analysed by EPMA. (a) Histogram of S contents (in at.%)
889 of BMS. Note that SS2-1 and SS2-4 refer to the same eclogite xenolith (SS2, from Kiseeva et al., 2017b)
890 but different polished thin sections. (b) Fe– Ni(+Co)–Cu ternary diagrams showing eclogite xenoliths
891 from this study in comparison to Roberts Victor eclogite xenoliths from Gréau et al. (2013) and BMS

892 inclusions in diamonds (Deines & Harris, 1995). (c) Cu–Fe–S diagram for chalcopyrite analysed during
893 this study in comparison to compositions from Gréau et al. (2013) and end-member chalcopyrite.
894 Abbreviations are chalcopyrite (Cp), pyrite with varying Ni content ($\text{Py} \pm \text{Ni}$), pyrrhotite (Po),
895 pentlandite (Pn), smythite-violarite (Smy-Vi) E-type diamond inclusion (E-Di) and P-type diamond
896 inclusion (P-Di).

897 **Figure 5** – Scatter plots for total PGE vs. various indicators of BMS major element composition and/or
898 dominant end-member sulphide mineral – (a) $\text{Ni}/(\text{Ni}+\text{Cu}+\text{Fe})$ and (b) $\text{Cu}/(\text{Cu}+\text{Ni}+\text{Fe})$. All Roberts Victor
899 eclogite xenoliths (RV-IM-xx and SS2) have been plotted in comparison to BMS inclusions within
900 eclogitic (E-type) and peridotitic (P-type) diamonds (data for Orapa (E-type, McDonald et al., 2017),
901 Diavik (E-type, Aulbach et al., 2012), and Mir and Udachnaya (P-type, Bulanova et al., 1996)), BMS in
902 mid-ocean ridge basalts (MORB) from Patten et al. (2013), and BMS inclusions in MORB (picritic lavas)
903 from Savelyev et al. (2018).

904 **Figure 6** – Chondrite-normalised PGE and Au spidergrams of BMS from the Roberts Victor eclogite
905 xenoliths (RV-IM-xx and SS2), with comparison plot of base metal sulphide (BMS) inclusions within
906 eclogitic (E-type) and peridotitic (P-type) diamonds (data from McDonald et al., 2017; Aulbach et al.,
907 2012 and Bulanova et al., 1996), BMS in mid-ocean ridge basalts (MORB) from Patten et al. (2013),
908 BMS inclusions in MORB (picritic lavas) from Savelyev et al. (2018), and BMS in mid-ocean ridge (MOR)
909 peridotites from Alard et al. (2005). All diagrams have been normalised to chondrite values from
910 Fischer-Gödde et al. (2010). Note that the eclogite xenolith data (this study) have been plotted
911 according to the corresponding Ni, Cu and Fe contents per LA-ICP-MS analyses to investigate the effect
912 of BMS major element composition on PGE-Au-Re contents. Thus, the following categories were used:
913 *Fe-(Ni,Cu) BMS* for analyses where both Ni and Cu occurred at < 10 wt.% each, *Ni,Fe-(Cu) BMS* for
914 analyses with ≥ 10 wt.% Ni and < 10 wt.% Cu, and *Cu,Fe-(Ni) BMS* for analyses with ≥ 10 wt.% Cu and
915 < 10 wt.% Ni. One analysis contained almost equal abundances of Ni and Cu (approximately 10 wt.%
916 of each) and has been labelled *Ni,Cu,Fe BMS*.

917 **Figure 7** – Bivariate trace element diagrams for BMS measured by LA-ICP-MS. (a) total PGE vs. S/Se,
918 (b) Pd vs. Se, and (c) S/Se vs. Au. (c) and (d) explore range of Te concentrations with Se and Au,
919 respectively. (e) chondrite-normalised Re/Os ratio ($(\text{Re/Os})_N$) vs. Os. All Roberts Victor eclogite
920 xenoliths (RV-IM-xx and SS2) have been plotted in comparison to BMS inclusions within eclogitic (E-
921 type) and peridotitic (P-type) diamonds using data from McDonald et al., (2017), Aulbach et al. (2012)
922 and Bulanova et al. (1996), BMS in mid-ocean ridge basalts (MORB) from Patten et al. (2013), and BMS
923 inclusions in MORB (picritic lavas) from Savelyev et al. (2018). Additional Re and Os data from
924 Richardson et al. (2001, 2004), McKenna (2001) and Simelane (2004) for diamond inclusions, and BMS
925 in mid-ocean ridge (MOR) peridotites from Alard et al. (2005).

926 **Figure 8** – Summary of chondrite-normalised PGE and Au spidergrams showing four main
927 compositional groups of BMS from the Roberts Victor eclogite xenoliths in this study: Types *i*, *ii*, *iii* and
928 *iv*. Comparison is made to Burness et al. (2020).

929 **Figure 9** – Trace element modelling of batch partial melting of Roberts Victor eclogite BMS as shown
930 by chondrite normalised (Fischer-Gödde et al., 2010) Ni, PGE, Au, Re and Cu spidergrams for silicate
931 melts generated by (a) different starting compositions of mantle BMS (as defined by the four end-
932 member BMS compositions identified for Roberts Victor, see Section 4.1) and (b) mixtures of BMS end-
933 members. In all models, we have assumed 100% BMS extraction from the source during melting and
934 used an initial starting proportion of 0.5% (by volume) of BMS in the eclogite source. Note that in (a),
935 a mean Roberts Victor BMS composition have been calculated from LA-ICP-MS data for all Roberts
936 Victor eclogite xenoliths analysed in this study, excluding the PGE-rich samples of RV-IM-02. In (b),
937 end-members *i* (based on mean from BMS in RV-IM-01, RV-IM-05, RV-IM-15 and SS2) and *ii* (based on
938 mean BMS composition from RV-IM-02) are mixed in ratios of 50:50, 80:20 and 95:5 (*i* : *ii*). All modelled
939 silicate melt compositions (coloured lines with diamond symbols) are plotted in comparison to the
940 parental magma compositions for the Bushveld (B1-3 and UM) from Barnes et al. (2010), plotted as
941 grey and black lines with circle symbols).

942 **Figure 10** – Trace element ratio and total PGE plots of melts derived from end-member Roberts Victor
943 eclogite xenolith BMS (calculated by the same method as Fig. 9a) in comparison to Bushveld parental
944 magmas (Barnes et al., 2010). (a) Pt/Pd ratio vs total PGE concentration, (b) Pt/Pd ratio vs Ni/Cu ratio,
945 and (c) Pt/Pd ratio vs Re/Os ratio. Note that in (c), the lack of Re data for the Bushveld parental
946 magmas (at the time of writing) mean that we cannot make a direct comparison to B1-3 and UM for
947 Re/Os. Instead we use the ‘Bushveld primary melt’ of McCandless & Ruiz (1991). Also shown are the
948 Re/Os ratios of gabbroic and basaltic eclogites from the Zermatt-Saas ophiolite terrain (Dale et al.,
949 2009) in lilac lines, the range of Re/Os ratios of BMS in eclogite xenoliths from Diavik (Slave Craton)
950 (Aulbach et al., 2009) as a grey bar, the chondritic composition of Fischer-Gödde et al. (2010) (black
951 circle), and the composition of Pyrolite from McDonough and Sun (1995) (grey circle).

952 **Table captions**

953 **Table 1** – Characteristics of mantle eclogite samples. All eclogites used in this study are classed as type
954 I – see text for details. Texture classifications based on McGregor and Carter (1970). *See Kiseeva et
955 al. (2017b) for further details on silicate chemistry and textures.

956 **Table 2** – Relative proportions of base metal sulphides (by area %) analysed by QEMSCAN.

957 **Table 3** – Summary of major element compositions of sulphides in Roberts Victor eclogite xenoliths
958 analysed *in situ* by EPMA.

959 **Table 4** – Summary of trace element compositions of analysed *in situ* by LA-ICP-MS. Full dataset in
960 Supplementary Material (including all major elements as measured by LA-ICP-MS). * for Ru, Rh and Pd
961 indicates abundances are reported for the element and have been corrected for isotope overlaps with
962 argide species. The following categories were used: *Fe-(Ni,Cu) BMS* for analyses where both Ni and Cu
963 occurred at < 10 wt.% each, *Ni,Fe-(Cu) BMS* for analyses with ≥ 10 wt.% Ni and < 10 wt.% Cu, and
964 *Cu,Fe-(Ni) BMS* for analyses with ≥ 10 wt.% Cu and < 10 wt.% Ni. Sample SS-2 had a restricted range
965 of BMS major elements compositions equivalent to pyrite with variable but low Ni and Cu
966 concentrations and has therefore been labelled *Py (± Ni,Cu)*.

967 ** Se concentration based on ⁸²Se isotope for these samples (as opposed to ⁷⁷Se for all others).

968 **Table 5** – Count (*n*) of interstitial vs included (and embayed) BMS in eclogite xenoliths from this study
969 and percentages of each per sample. No data available for RV-IM-01 and RV-IM-17.

970

971 **Supplementary material**

972 **Table A** – Mineral association data for samples analysed by QEMSCAN

973 **Table B** – Standards used for EPMA and lower limits of detection (LLD)

974 **Table C** – Standards used for LA-ICP-MS and detection limits.

975 **Table D** – Full EPMA sulphide data analysed by WDS. Standard information available in Table B.

976 **Table E** – Full LA-ICP-MS data for all sulphides analysed in this study. Note that ‘–’ denotes “isotope
977 not measured”; * Denotes isotopes which have been interference-corrected (Standard 1, Cardiff
978 University, matrix matched) for argide species and Cd; ** Se concentration based on ⁸²Se isotope for
979 these samples (as opposed to ⁷⁷Se for all others). Values in *italic font* indicate those below detection
980 limit, but stated as 50% detection limit to allow for plotting. Standard information available in Table
981 C.

982 **Figure A** – Silicate mineral chemistry. Ternary diagrams for sample RV-IM-15. (a) end-member
983 compositions of garnet (Pyp pyropem, GRS grossular, Alm almandine). (b) end-member compositions
984 of primary omphacitic clinopyroxenes (red), secondary Al-diopside (blue) and comparison to Roberts
985 Victor eclogite xenolith clinopyroxenes from Huang et al. (2012) (green) (Jd jadite, Aeg aegerine).

986 **Figure B** – All QEMSCAN field scans of BMS. (a) RV-IM-15 C Irregular BMS interstitial to garnet and
987 pervasive Al-diopside. The mss (pyrite/pyrrhotite) core can be clearly seen, as well as pentlandite
988 forming along internal fractures and forming an inner rim, chalcocopyrite is forming the blocky outer
989 rim. (b) RV-IM-15 G Highly deteriorated BMS interstitial to clinopyroxenes and an albite vein. This BMS
990 lacks a distinct mss core and is solely composed of pentlandite and chalcocopyrite. (c) RV-IM-15 E
991 Rounded BMS embayment in garnet. The fracture it sits within is predominantly secondary
992 clinopyroxene and biotite. The BMS has a mss core with pentlandite forming as internal fractures and
993 flames. In this BMS, pentlandite forms the dominant outer phase, with only minor chalcocopyrite. (d)
994 RV-IM-18 D Rounded BMS semi-enclosed within the rim of a garnet. The BMS is within a fracture
995 within garnet, primarily infilled with chlorite. (e) RV-IM-18 C Rounded BMS enclosed within the same
996 garnet as (d), but located slightly further away from the rim. Mostly mss with minor blocky pentlandite
997 and chalcocopyrite rim. Within the garnet there are inclusions and fractures containing chlorite, albite
998 and biotite.

999 **Figure C** – Time resolved analysis (TRA) plots of a selection of BMS analysed by LA-ICP-MS. TRA
1000 includes switch-off of the laser (white area after ‘sample’) and gas blank at the end of the analysis
1001 (grey area on the right hand side of each plot). Area of sample analysis (labelled ‘sample’ and

1002 interpolated for processing of LA-ICP-MS data) is delineated. (a) RV-IM-17 BMS1 and (b) RV-IM-01
1003 BMS1B. Both sets of TRA show mixed sulphides, zoned in Cu (such that RV-IM-17 BMS1 demonstrates
1004 classic texture of chalcopyrite at the rim of the BMS grain and mss in the centre). RV-IM-01 BMS1B
1005 shows more complex zonation of end-member sulphides with enrichment in Zn in the centre. Zonation
1006 in As and Ag appear in both TRA sets. PGE are present in higher concentrations in RV-IM-01 BMS1B
1007 and particularly this TRA set demonstrates PGM (probably as nano-nuggets) at the rims of the BMS
1008 grain.

1009 **Figure D** – Further bivariate plots of LA-ICP-MS data from BMS. Data are plotted according to sample
1010 number only. Corresponding data table is available in Table E of this supplementary dataset.

1011 **Figure E** – SEM BSE images of Ni-arsenide and PGM.

1012 **Figure F** – Trace element modelling of batch partial melting of Roberts Victor eclogite BMS. The top
1013 four panels show the concentration (chondrite normalised using the values of Fischer-Gödde et al.,
1014 2010) of Ni, PGE, Au, Re and Cu in the silicate melt generated at different degrees of partial melting
1015 of the BMS in the source (where F = melt fraction), according to different starting compositions. Each
1016 panel (top four models) use a starting composition from each of the four end-member BMS
1017 compositions identified in the Roberts Victor xenoliths analysed in this study (see Section 4.1). Note
1018 that due to the highly chalcophile behaviour of the PGE, > 99% of BMS ($F = 0.999$) must be extracted
1019 used from the source in order for the silicate melt to have a composition similar to the Bushveld
1020 parental magma compositions (B1-3 and UM). These top four models (shades of purple lines) were
1021 conducted assuming 0.5% (by volume) BMS in the source. The bottom panel of this figure (shades of
1022 red lines) shows modelling to demonstrate the effect of complete melting and extraction of the mean
1023 BMS composition of the Roberts Victor eclogite xenoliths (this study) but at different abundances of
1024 BMS in the mantle source (0.03 to 1 % BMS by volume). In summary, a higher abundance of BMS in
1025 the source leads to a higher concentration of chalcophile elements in the resulting silicate melt. Note
1026 that the mean Roberts Victor eclogitic BMS composition was calculated excluding the rare high-PGE
1027 BMS from RV-IM-02.

1028 **References**

- 1029 Ahmed, A.H., Arai, S. and Ikenne, M., 2009. Mineralogy and paragenesis of the Co-Ni
 1030 arsenide ores of Bou Azzer, Anti-Atlas, Morocco. *Economic Geology*, 104(2), pp.249-
 1031 266.
- 1032 Alard O., Griffin W. L., Lorand, J.-P., E., Jackson S.E., O'Reilly S. Y., 2000. Non-chondritic
 1033 distribution of the highly siderophile elements in mantle sulphides. *Nature*, 407, pp.
 1034 891–894.
- 1035 Alard, O., Luguët, A., Pearson, N.J., Griffin, W.L., Lorand, J.P., Gannoun, A., Burton, K.W. and
 1036 O'Reilly, S.Y., 2005. In situ Os isotopes in abyssal peridotites bridge the isotopic gap
 1037 between MORBs and their source mantle. *Nature*, 436(7053), pp.1005-1008.
- 1038 Alard, O., Lorand, J.P., Reisberg, L., Bodinier, J.L., Dautria, J.M., O'reilly, S.Y., 2011. Volatile-
 1039 rich metasomatism in montferrier xenoliths (Southern France): Implications for the
 1040 abundances of chalcophile and highly siderophile elements in the subcontinental
 1041 mantle. *Journal of Petrology*, 52, pp. 2009–2045.
- 1042 Aulbach, S., Creaser, R.A., Pearson, N.J., Simonetti, S.S., Heaman, L.M., Griffin, W.L., Stachel,
 1043 T., 2009. Sulfide and whole rock Re-Os systematics of eclogite and pyroxenite
 1044 xenoliths from the Slave Craton, Canada. *Earth and Planetary Science Letters*, 283,
 1045 pp. 48–58.
- 1046 Aulbach, S., Stachel, T., Heaman, L.M., Creaser, R.A. and Shirey, S.B., 2010. Formation of
 1047 cratonic subcontinental lithospheric mantle from hybrid plume sources. *Geochimica
 1048 et Cosmochimica Acta*, 74(12, Supplement), pp. A37-A37.
- 1049 Aulbach, S., Stachel, T., Heaman, L.M., Creaser, R.A. and Shirey, S.B., 2011. Formation of
 1050 cratonic subcontinental lithospheric mantle and complementary komatiite from
 1051 hybrid plume sources. *Contributions to Mineralogy and Petrology*, 161(6), pp.947-
 1052 960.
- 1053 Aulbach, S., Stachel, T., Seitz, H.M., Brey, G.P., 2012. Chalcophile and siderophile elements in
 1054 sulphide inclusions in eclogitic diamonds and metal cycling in a Paleoproterozoic
 1055 subduction zone. *Geochimica et Cosmochimica Acta*, 93, pp. 278-299.
- 1056 Aulbach, S., Jacob, D.E., 2016. Major- and trace-elements in cratonic mantle eclogites and
 1057 pyroxenites reveal heterogeneous sources and metamorphic processing of low-
 1058 pressure protoliths. *Lithos*, 262, pp. 586–605.
- 1059 Aulbach, S., Mungall, J.E., Pearson, D.G., 2016. Distribution and processing of highly
 1060 siderophile elements in cratonic mantle lithosphere. *Reviews in Mineralogy and
 1061 Geochemistry* 81 (1), pp. 239–304.
- 1062 Aulbach, S., Jacob, D.E., Cartigny, P., Stern, R.A., Simonetti, S.S., Wörner, G., Viljoen, K.S.,
 1063 2017. Eclogite xenoliths from Orapa: Ocean crust recycling, mantle metasomatism
 1064 and carbon cycling at the western Zimbabwe craton margin. *Geochimica et
 1065 Cosmochimica Acta* 213, pp. 574–592.
- 1066 Barnes, S.J., Maier, W.D. and Curl, E.A., 2010. Composition of the marginal rocks and sills of
 1067 the Rustenburg Layered Suite, Bushveld Complex, South Africa: implications for the
 1068 formation of the platinum-group element deposits. *Economic Geology*, 105(8),
 1069 pp.1491-1511.
- 1070 Barnes, S.J., Mungall, J.E., Maier, W.D., 2015. Platinum group elements in mantle melts and
 1071 mantle samples. *Lithos*, 232: 395-417.
- 1072 Becker, H., Horan, M.F., Walker, R.J., Gao, S., Lorand, J.P. and Rudnick, R.L., 2006. Highly
 1073 siderophile element composition of the Earth's primitive upper mantle: constraints

1074 from new data on peridotite massifs and xenoliths. *Geochimica et Cosmochimica*
1075 *Acta*, 70(17), pp.4528-4550.

1076 Bockrath, C., Ballhaus, C. and Holzheid, A., 2004. Fractionation of the platinum-group
1077 elements during mantle melting. *Science*, 305(5692), pp.1951-1953.

1078 Brenan, J.M., 2015. Se–Te fractionation by sulfide–silicate melt partitioning: implications for
1079 the composition of mantle-derived magmas and their melting residues. *Earth and*
1080 *Planetary Science Letters*, 422, pp.45-57.

1081 Brenan, J.M. and Andrews, D., 2001. High-temperature stability of laurite and Ru–Os–Ir alloy
1082 and their role in PGE fractionation in mafic magmas. *The Canadian Mineralogist*,
1083 39(2), pp.341-360.

1084 Brey, G.P., Shu, Q., 2018. The birth, growth and ageing of the Kaapvaal subcratonic mantle.
1085 *Mineralogy and Petrology*, 112, pp. 23–41.

1086 Bulanova, G.P., Griffin, W.L., Ryan, C.G., Shestakova, O.Y., Barnes, S.J., 1996. Trace elements
1087 in sulfide inclusions from Yakutian diamonds. *Contributions to Mineralogy and*
1088 *Petrology*, 124(2), pp. 111-125.

1089 Burness, S., Smart, K.A., Tappe, S., Stevens, G., Woodland, A.B., Cano, E., 2020. Sulphur-rich
1090 mantle metasomatism of Kaapvaal craton eclogites and its role in redox-controlled
1091 platinum group element mobility. *Chemical Geology*, 542.

1092 Choi, E., Fiorentini, M.L., Hughes, H.S. and Giuliani, A., 2020. Platinum-group element and
1093 Au geochemistry of Late Archean to Proterozoic calc-alkaline and alkaline magmas in
1094 the Yilgarn Craton, Western Australia. *Lithos*, 374, p.105716.

1095 Coggon, J.A., Nowell, G.M., Pearson, D.G., Oberthür, T., Lorand, J.P., Melcher, F. and
1096 Parman, S.W., 2012. The 190Pt–186Os decay system applied to dating platinum-
1097 group element mineralization of the Bushveld Complex, South Africa. *Chemical*
1098 *Geology*, 302, pp.48-60.

1099 Dale, C.W., Burton, K.W., Pearson, D.G., Gannoun, A., Alard, O., Argles, T.W. and Parkinson,
1100 I.J., 2009. Highly siderophile element behaviour accompanying subduction of oceanic
1101 crust: whole rock and mineral-scale insights from a high-pressure terrain.
1102 *Geochimica et Cosmochimica Acta*, 73(5), pp.1394-1416.

1103 De Wit, M.J., De Ronde, C.E.J., Tredoux, M., Roering, C., Hart, R.J., Armstrong, R.A., Green,
1104 R.W.E., Peberdy, E., Hart, R.A., 1992. Formation of an Archaean continent. *Nature*,
1105 357, pp. 553–562.

1106 Deines, P., Harris, J.W., 1995. Sulfide inclusion chemistry and carbon isotopes of African
1107 diamonds. *Geochimica et Cosmochimica Acta*, 59, pp. 3173-3188.

1108 Delpech, G., Lorand, J.-P., Grégoire, M., Cottin, J.-Y., O'Reilly, S.Y., 2012. In-situ geochemistry
1109 of sulfides in highly metasomatized mantle xenoliths from Kerguelen, southern
1110 Indian Ocean. *Lithos*, 154, pp. 296–314.

1111 Dreibus, G., Palme, H., Spettel, B., Zipfel, J. and Wänke, H., 1995. Sulfur and selenium in
1112 chondritic meteorites. *Meteoritics*, 30(4), pp.439-445.

1113 Eggler, D.H., Lorand, J.P., 1993. Mantle sulfide geobarometry. *Geochimica et Cosmochimica*
1114 *Acta*, 57 (10), 2213–2222.

1115 Eriksson, P.G., Rigby, M.J., Bandopadhyay, P.C., Steenkamp, N.C., 2011. The Kaapvaal
1116 Craton, South Africa: no evidence for a supercontinental affinity prior to 2.0 Ga?
1117 *International Geology Review*, 53, pp. 1312–1330.

1118 Ferraris, C., Lorand, J.-P., 2014. Novodneprite (AuPb₃), anyuiite [Au(Pb, Sb)₂] and gold
1119 micro- and nano-inclusions within plastically deformed mantle-derived olivine from

1120 the Lherz peridotite (Pyrenees, France): a HRTEM–AEM–EELS study. *Physics and*
1121 *Chemistry of Minerals*, 42 (2), 143–150.

1122 Field, M., Stiefenhofer, J., Robey, J. and Kurszlauskis, S., 2008. Kimberlite-hosted diamond
1123 deposits of southern Africa: a review. *Ore Geology Reviews*, 34(1-2), pp.33-75.

1124 Fischer-Gödde, M., Becker, H. and Wombacher, F., 2010. Rhodium, gold and other highly
1125 siderophile element abundances in chondritic meteorites. *Geochimica et*
1126 *Cosmochimica Acta*, 74(1), pp.356-379.

1127 Fung, A.T., Haggerty, S.E., 1995. Petrography and mineral compositions of eclogites from the
1128 Koidu kimberlite complex, Sierra-Leone. *Journal of Geophysical Research-Solid Earth*,
1129 100(B10), pp. 20451-20473.

1130 Good, N., De Wit, M.J., 1997. The Thabazimbi-Murchison lineament of the Kaapvaal Craton,
1131 South Africa: 2700 Ma of episodic deformation. *Journal of the Geological Society*,
1132 154, pp. 93–97.

1133 Goodall, W.R. and Scales, P.J., 2007. An overview of the advantages and disadvantages of
1134 the determination of gold mineralogy by automated mineralogy. *Minerals*
1135 *Engineering*, 20(5), pp.506-517.

1136 Goodall, W.R., Scales, P.J. and Butcher, A.R., 2005. The use of QEMSCAN and diagnostic
1137 leaching in the characterisation of visible gold in complex ores. *Minerals Engineering*,
1138 18(8), pp.877-886.

1139 Gottlieb, P., Wilkie, G., Sutherland, D., Ho-Tun, E., Suthers, S., Perera, K., Jenkins, B.,
1140 Spencer, S., Butcher, A. and Rayner, J., 2000. Using quantitative electron microscopy
1141 for process mineralogy applications. *The Journal of the Minerals, Metals and*
1142 *Materials Society*, 52, pp.24–25.

1143 Gréau, Y., 2011. Siderophile and chalcophile elements in Roberts Victor eclogites: insights on
1144 the generation of mantle heterogeneity (Doctoral dissertation, Macquarie
1145 University).

1146 Gréau, Y., Alard, O., Griffin, W.L., Huang, J.X., O'Reilly, S.Y., 2013. Sulfides and chalcophile
1147 elements in Roberts Victor eclogites: Unravelling a sulfide-rich metasomatic event.
1148 *Chemical Geology*.

1149 Gréau, Y., Griffin, W.L., Alard, O. and O'Reilly, S.Y., 2008, October. Petrology and
1150 geochemistry of eclogitic sulphides: a new insight on origin of mantle eclogites?. In
1151 *International Kimberlite Conference: Extended Abstracts*, 9.

1152 Green, D.H., Hibberson, W.O., Kovacs, I., Rosenthal, A., 2010. Water and its influence on the
1153 lithosphere-asthenosphere boundary. *Nature*, 467(7314), pp. 448-451.

1154 Griffin, W.L., O'Reilly, S.Y., 2007. Cratonic lithospheric mantle: Is anything subducted?, in:
1155 *Episodes*, pp. 43–53.

1156 Griffin, W.L., O'Reilly, S.Y., Abe, N., Aulbach, S., Davies, R.M., Pearson, N.J., Doyle, B.J., Kivi,
1157 K., 2003a. The origin and evolution of Archean lithospheric mantle. *Precambrian*
1158 *Research*, 127, pp. 19–41.

1159 Griffin, W.L., O'Reilly, S.Y., Natapov, L.M., Ryan, C.G., 2003b. The evolution of lithospheric
1160 mantle beneath the Kalahari Craton and its margins. *Lithos*, 71: 215–241.

1161 Gurney, J.J. and Kirkley, M.B., 1996. Kimberlite dyke mining in South Africa. *Africa*
1162 *Geoscience Review*, 3(2), pp. 191-201.

1163 Harris, C., Pronost, J.J., Ashwal, L.D. and Cawthorn, R.G., 2005. Oxygen and hydrogen
1164 isotope stratigraphy of the Rustenburg Layered Suite, Bushveld Complex: constraints
1165 on crustal contamination. *Journal of Petrology*, 46(3), pp.579-601.

- 1166 Hart, S.R. and Kinloch, E.D., 1989. Osmium isotope systematics in Witwatersrand and
1167 Bushveld ore deposits. *Economic Geology*, 84(6), pp.1651-1655.
- 1168 Harte, B. and Gurney, J.J., 1975. Evolution of clinopyroxene and garnet in an eclogite nodule
1169 from the Roberts Victor kimberlite pipe, South Africa. In *Physics and Chemistry of the*
1170 *Earth*, pp. 367-387. Pergamon.
- 1171 Harvey, J., König, S. and Luguet, A., 2015. The effects of melt depletion and metasomatism
1172 on highly siderophile and strongly chalcophile elements: S–Se–Te–Re–PGE
1173 systematics of peridotite xenoliths from Kilbourne Hole, New Mexico. *Geochimica et*
1174 *Cosmochimica Acta*, 166, pp.210-233.
- 1175 Hatton, C.J., 1995. Mantle plume origin for the Bushveld and Ventersdorp magmatic
1176 provinces. *Journal of African Earth Sciences*, 21(4), pp.571-577.
- 1177 Hatton, C.J. and Gurney, J.J., 1977, September. A diamond graphite eclogite from the
1178 Roberts Victor Mine. In *International Kimberlite Conference: Extended Abstracts*, 2,
1179 pp. 141-143.
- 1180 Heaman, L.M., Creaser, R.A., Cookenboo, H.O., Chacko, T., 2006. Multi-stage modification of
1181 the northern Slave mantle lithosphere: evidence from zircon- and diamond-bearing
1182 eclogite xenoliths entrained in Jericho kimberlite, Canada. *Journal of Petrology*,
1183 47(4), pp. 821-858.
- 1184 Helmy, H.M., Ballhaus, C., Berndt, J., Bockrath, C., Wohlgemuth-Ueberwasser, C., 2007.
1185 Formation of Pt, Pd and Ni tellurides: experiments in sulfide-telluride systems.
1186 *Contributions to Mineralogy and Petrology*, 153, pp. 577–591.
- 1187 Herzberg, C., Zhang, J.Z., 1996. Melting experiments on anhydrous peridotite KLB-1:
1188 Compositions of magmas in the upper mantle and transition zone. *Journal of*
1189 *Geophysical Research-Solid Earth*, 101(B4), pp. 8271-8295.
- 1190 Hills, D.V., Haggerty, S.E., 1989. Petrochemistry of eclogites from the Koidu kimberlite
1191 complex, Sierra-Leone. *Contributions to Mineralogy and Petrology*, 103(4), pp. 397-
1192 422.
- 1193 Holwell, D.A., McDonald, I., 2010. A review of the behaviour of platinum group elements
1194 within natural magmatic sulfide ore systems. *Platinum Metals Review*, 54, pp. 26–36.
- 1195 Holwell, D.A., Adeyemi, Z., Ward, L.A., Smith, D.J., Graham, S.D., McDonald, I. and Smith,
1196 J.W., 2017. Low temperature alteration of magmatic Ni-Cu-PGE sulfides as a source
1197 for hydrothermal Ni and PGE ores: A quantitative approach using automated
1198 mineralogy. *Ore Geology Reviews*, 91, pp.718-740.
- 1199 Holwell, D.A., Fiorentini, M., McDonald, I., Lu, Y., Giuliani, A., Smith, D.J., Keith, M. and
1200 Locmelis, M., 2019. A metasomatized lithospheric mantle control on the
1201 metallogenic signature of post-subduction magmatism. *Nature communications*,
1202 10(1), pp.1-10.
- 1203 Huang, J.X., Gréau, Y., Griffin, W.L., O'Reilly, S.Y. and Pearson, N.J., 2012. Multi-stage origin
1204 of Roberts Victor eclogites: progressive metasomatism and its isotopic effects.
1205 *Lithos*, 142, pp.161-181.
- 1206 Huang, J.X., Li, P., Griffin, W.L., Xia, Q.K., Gréau, Y., Pearson, N.J. and O'Reilly, S.Y., 2014.
1207 Water contents of Roberts Victor xenolithic eclogites: primary and metasomatic
1208 controls. *Contributions to Mineralogy and Petrology*, 168(6), p.1092.
- 1209 Hughes, H.S., McDonald, I. and Kerr, A.C., 2015. Platinum-group element signatures in the
1210 North Atlantic Igneous Province: implications for mantle controls on metal budgets
1211 during continental breakup. *Lithos*, 233, pp.89-110.

- 1212 Hughes, H.S., McDonald, I., Loocke, M., Butler, I.B., Upton, B.G. and Faithfull, J.W., 2017.
 1213 Paradoxical co-existing base metal sulphides in the mantle: the multi-event record
 1214 preserved in Loch Roag peridotite xenoliths, North Atlantic Craton. *Lithos*, 276,
 1215 pp.103-121.
- 1216 Jacob, D.E., 2004. Nature and origin of eclogite xenoliths from kimberlites. *Lithos*, 77(1-4),
 1217 pp. 295-316.
- 1218 James, D.E., Boyd, F.R., Schutt, D., Bell, D.R., Carlson, R.W., 2004. Xenolith constraints on
 1219 seismic velocities in the upper mantle beneath southern Africa. *Geochemistry
 1220 Geophysics Geosystems*, 5.
- 1221 Jacob, D.E., Schmickler, B. and Schulze, D.J., 2003. Trace element geochemistry of coesite-
 1222 bearing eclogites from the Roberts Victor kimberlite, Kaapvaal craton. *Lithos*, 71(2-
 1223 4), pp.337-351.
- 1224 Jacob, D.E., Bizimis, M. and Salters, V.J.M., 2005. Lu–Hf and geochemical systematics of
 1225 recycled ancient oceanic crust: evidence from Roberts Victor eclogites. *Contributions
 1226 to Mineralogy and Petrology*, 148(6), pp.707-720.
- 1227 Jelsma, H., Barnett, W., Richards, S., Lister, G., 2009. Tectonic setting of kimberlites. *Lithos*,
 1228 112, pp. 155–165.
- 1229 Kiseeva, E.S., Fonseca, R.O.C., Smythe, D.J., 2017a. Chalcophile elements and sulfides in the
 1230 upper mantle. *Elements*, 13(2), pp. 111-116.
- 1231 Kiseeva, E.S., Kamenetsky, V.S., Yaxley, G.M., Shee, S.R., 2017b. Mantle melting versus
 1232 mantle metasomatism - "The chicken or the egg" dilemma. *Chemical Geology*, 455,
 1233 pp. 120-130.
- 1234 König, S., Luguët, A., Lorand, J.P., Wombacher, F. and Lissner, M., 2012. Selenium and
 1235 tellurium systematics of the Earth's mantle from high precision analyses of ultra-
 1236 depleted orogenic peridotites. *Geochimica et Cosmochimica Acta*, 86, pp.354-366.
- 1237 Kramers, J.D., 1979. Lead, uranium, strontium, potassium and rubidium in inclusion-bearing
 1238 diamonds and mantle-derived xenoliths from southern Africa. *Earth and Planetary
 1239 Science Letters*, 42(1), pp.58-70.
- 1240 Krogh, E.J., 1988. The garnet–clinopyroxene Fe/Mg geothermometer—a reinterpretation of
 1241 existing experimental data. *Contributions to Mineralogy and Petrology*, 99, pp. 44–
 1242 48.
- 1243 Locmelis, M., Fiorentini, M.L., Barnes, S.J. and Pearson, N.J., 2013. Ruthenium variation in
 1244 chromite from komatiites and komatiitic basalts—a potential mineralogical indicator
 1245 for nickel sulfide mineralization. *Economic Geology*, 108(2), pp.355-364.
- 1246 Lorand, J.-P., Alard, O., 2010. Determination of selenium and tellurium concentrations in
 1247 Pyrenean peridotites (Ariege, France): new insight into S/Se/Te systematics of the
 1248 upper in mantle samples. *Chemical Geology* 278, pp. 120–130.
- 1249 Lorand, J.P., Alard, O., Luguët, A., Keays, R.R., 2003. Sulfur and selenium systematics of the
 1250 subcontinental lithospheric mantle: Inferences from the Massif Central xenolith suite
 1251 (France). *Geochimica et Cosmochimica Acta*.
- 1252 Lorand, J.-P., Grégoire, M., 2006. Petrogenesis of basemetal sulphide assemblages of some
 1253 peridotites from the Kaapvaal craton (South Africa). *Contributions to Mineralogy and
 1254 Petrology* 151 (5), pp. 521–538.
- 1255 Lorand, J.P. and Luguët, A., 2016. Chalcophile and siderophile elements in mantle rocks:
 1256 Trace elements controlled by trace minerals. *Reviews in Mineralogy and
 1257 Geochemistry*, 81(1), pp.441-488.

- 1258 Lorand, J.P., Alard, O. and Luguët, A., 2010. Platinum-group element micronuggets and
 1259 refertilization process in Lherz orogenic peridotite (northeastern Pyrenees, France).
 1260 Earth and Planetary Science Letters, 289(1-2), pp.298-310.
- 1261 Lorand, J.P., Luguët, A. and Alard, O., 2013. Platinum-group element systematics and
 1262 petrogenetic processing of the continental upper mantle: A review. *Lithos*, 164, pp.2-
 1263 21.
- 1264 Luguët, A. and Reisberg, L., 2016. Highly siderophile element and ¹⁸⁷O_s signatures in non-
 1265 cratonic basalt-hosted peridotite xenoliths: Unravelling the origin and evolution of
 1266 the post-Archean lithospheric mantle. *Reviews in Mineralogy and Geochemistry*,
 1267 81(1), pp.305-367.
- 1268 MacGregor, I.D. and Manton, W.I., 1986. Roberts Victor eclogites: ancient oceanic crust.
 1269 *Journal of Geophysical Research: Solid Earth*, 91(B14), pp.14063-14079.
- 1270 Manton, W.I. and Tatsumoto, M., 1971. Some Pb and Sr isotopic measurements on eclogites
 1271 from the Roberts Victor mine, South Africa. *Earth and Planetary Science Letters*,
 1272 10(2), pp.217-226.
- 1273 Macgregor, I.D. and Carter, J.L., 1970. The chemistry of clinopyroxenes and garnets of
 1274 eclogite and peridotite xenoliths from the Roberts Victor mine, South Africa. *Physics*
 1275 *of the Earth and Planetary Interiors*, 3, pp.391-397.
- 1276 McCandless, T.E. and Ruiz, J., 1991. Osmium isotopes and crustal sources for platinum-group
 1277 mineralization in the Bushveld Complex, South Africa. *Geology*, 19(12), pp.1225-
 1278 1228.
- 1279 McLean, H., Banas, A., Creighton, S., Whiteford, S., Luth, R.W. and Stachel, T., 2007. Garnet
 1280 xenocrysts from the Diavik mine, NWT, Canada: Composition, color, and paragenesis.
 1281 *The Canadian Mineralogist*, 45(5), pp.1131-1145.
- 1282 McDonald, I. and Viljoen, K.S., 2006. Platinum-group element geochemistry of mantle
 1283 eclogites: a reconnaissance study of xenoliths from the Orapa kimberlite, Botswana.
 1284 *Applied Earth Science*, 115(3), pp.81-93.
- 1285 McDonough, W.F. and Sun, S.S., 1995. The composition of the Earth. *Chemical geology*,
 1286 120(3-4), pp.223-253.
- 1287 Miller, W.G., Holland, T.J. and Gibson, S.A., 2016. Garnet and spinel oxybarometers: new
 1288 internally consistent multi-equilibria models with applications to the oxidation state
 1289 of the lithospheric mantle. *Journal of Petrology*, 57(6), pp.1199-1222.
- 1290 Moore, A., Blenkinsop, T., Cotterill, F., 2008. Controls on post-Gondwana alkaline volcanism
 1291 in Southern Africa. *Earth and Planetary Science Letters*, 268, pp. 151–164.
- 1292 Mungall, J.E. and Brenan, J.M., 2014. Partitioning of platinum-group elements and Au
 1293 between sulfide liquid and basalt and the origins of mantle-crust fractionation of the
 1294 chalcophile elements. *Geochimica et Cosmochimica Acta*, 125, pp.265-289.
- 1295 Naldrett, A.J., 2011. Fundamentals of magmatic sulfide deposits. *Reviews in Economic*
 1296 *Geology*, 17(1), pp. 1-50.
- 1297 Ongley, J.S., Basu, A.R. and Kyser, T.K., 1987. Oxygen isotopes in coexisting garnets,
 1298 clinopyroxenes and phlogopites of Roberts Victor eclogites: implications for
 1299 petrogenesis and mantle metasomatism. *Earth and Planetary Science Letters*, 83(1-
 1300 4), pp.80-84.
- 1301 Patten, C., Barnes, S.J., Mathez, E.A. and Jenner, F.E., 2013. Partition coefficients of
 1302 chalcophile elements between sulfide and silicate melts and the early crystallization
 1303 history of sulfide liquid: LA-ICP-MS analysis of MORB sulfide droplets. *Chemical*
 1304 *Geology*, 358, pp.170-188.

- 1305 Pitcher, L., Helz, R.T., Walker, R.J. and Piccoli, P., 2009. Fractionation of the platinum-group
1306 elements and Re during crystallization of basalt in Kilauea Iki Lava Lake, Hawaii.
1307 *Chemical Geology*, 260(3-4), pp.196-210.
- 1308 Prichard, H.M., Knight, R.D., Fisher, P.C., McDonald, I., Zhou, M.F. and Wang, C.Y., 2013.
1309 Distribution of platinum-group elements in magmatic and altered ores in the
1310 Jinchuan intrusion, China: an example of selenium remobilization by postmagmatic
1311 fluids. *Mineralium Deposita*, 48(6), pp.767-786.
- 1312 Richardson S.H., Shirey S.B., 2008. Continental mantle signature of Bushveld magmas and
1313 coeval diamonds. *Nature*, 453, pp. 910–913.
- 1314 Richardson S.H., Shirey S.B., Harris J.W., 2004. Episodic diamond genesis at Jwaneng,
1315 Botswana, and implications for Kaapvaal craton evolution. *Lithos* 77, pp. 143–154.
- 1316 Rollinson, G.K., Andersen, J.C., Stickland, R.J., Boni, M. and Fairhurst, R., 2011.
1317 Characterisation of non-sulphide zinc deposits using QEMSCAN®. *Minerals*
1318 *Engineering*, 24(8), pp.778-787.
- 1319 Saunders, J.E., Pearson, N.J., O'Reilly, S.Y., Griffin, W.L., 2015. Sulfide metasomatism and the
1320 mobility of gold in the lithospheric mantle. *Chemical Geology*, 410, pp. 149–161.
- 1321 Sautter, V. and Harte, B., 1988. Diffusion gradients in an eclogite xenolith from the Roberts
1322 Victor kimberlite pipe: 1. Mechanism and evolution of garnet exsolution in Al₂O₃-
1323 rich clinopyroxene. *Journal of Petrology*, 29(6), pp.1325-1352.
- 1324 Savelyev, D.P., Kamenetsky, V.S., Danyushevsky, L.V., Botcharnikov, R.E., Kamenetsky, M.B.,
1325 Park, J.W., Portnyagin, M.V., Olin, P., Krashennikov, S.P., Hauff, F. and Zelenski,
1326 M.E., 2018. Immiscible sulfide melts in primitive oceanic magmas: Evidence and
1327 implications from picrite lavas (Eastern Kamchatka, Russia). *American Mineralogist:*
1328 *Journal of Earth and Planetary Materials*, 103(6), pp.886-898.
- 1329 Schoenberg, R., Kruger, F.J., Nägler, T.F., Meisel, T. and Kramers, J.D., 1999. PGE enrichment
1330 in chromitite layers and the Merensky Reef of the western Bushveld Complex; a Re–
1331 Os and Rb–Sr isotope study. *Earth and Planetary Science Letters*, 172(1-2), pp.49-64.
- 1332 Shu, Q., Brey, G.P., Gerdes, A. and Hofer, H.E., 2013. Geochronological and geochemical
1333 constraints on the formation and evolution of the mantle underneath the Kaapvaal
1334 craton: Lu–Hf and Sm–Nd systematics of subcalcic garnets from highly depleted
1335 peridotites. *Geochimica et Cosmochimica Acta*, 113, pp.1-20.
- 1336 Schulze, D.J., 1989. Constraints on the abundance of eclogite in the upper mantle. *Journal of*
1337 *Geophysical Research-Solid Earth and Planets*, 94(B4), pp, 4205-4212.
- 1338 Schmitz, M.D., Bowring, S.A., de Wit, M.J., Gartz, V., 2004. Subduction and terrane collision
1339 stabilize the western Kaapvaal craton tectosphere 2.9 billion years ago. *Earth and*
1340 *Planetary Science Letters*, 222, pp. 363–376.
- 1341 Shirey, S.B., Richardson, S.H., 2011. Start of the Wilson cycle at 3 Ga shown by diamonds
1342 from subcontinental mantle. *Science*, 333, pp. 434–436.
- 1343 Simon, N.S.C., Carlson, R.W., Pearson, D.G., Davies, G.R., 2007. The origin and evolution of
1344 the Kaapvaal Cratonic Lithospheric Mantle. *Journal of Petrology*, 48, pp. 589–625.
- 1345 Smith, J.W., Holwell, D.A. and McDonald, I., 2014. Precious and base metal geochemistry
1346 and mineralogy of the Grasvalley Norite–Pyroxenite–Anorthosite (GNPA) member,
1347 northern Bushveld Complex, South Africa: implications for a multistage
1348 emplacement. *Mineralium Deposita*, 49(6), pp.667-692.
- 1349 Spandler, C., Yaxley, G., Green, D.H., Rosenthal, A., 2008. Phase relations and melting of
1350 anhydrous K-bearing eclogite from 1200 to 1600°C and 3 to 5 GPa. *Journal of*
1351 *Petrology*, 49(4), pp. 771-795.

- 1352 Stachel, T., Harris, J.W., 2008. The origin of cratonic diamonds - Constraints from mineral
1353 inclusions. *Ore Geology Reviews*, 34(1-2), pp. 5-32.
- 1354 Tappe, S., Smart, K., Torsvik, T., Massuyeau, M. and de Wit, M., 2018. Geodynamics of
1355 kimberlites on a cooling Earth: clues to plate tectonic evolution and deep volatile
1356 cycles. *Earth and Planetary Science Letters*, 484, pp.1-14.
- 1357 Thomassot, E., Farquhar, J., Bouden, N., Harris, J.W., McKeegan, K., Cliff, J., Wing, B. and
1358 Piccoli, P., 2017, September. The Archean sedimentary sulfur recycling under the
1359 Kaapvaal craton revisited from 4S-isotopic compositions in sulfide inclusions in
1360 diamonds from Kimberley Pool (South Africa) Jwaneng and Orapa (Botswana). In
1361 *International Kimberlite Conference: Extended Abstracts (Vol. 11)*.
- 1362 Walker, R.J., Carlson, R.W., Shirey, S.B., F.R, B., 1989. Os, Sr, Nd, and Pb isotope systematics
1363 of southern African peridotite xenoliths: Implications for the chemical evolution of
1364 subcontinental mantle. *Geochimica et Cosmochimica Acta*, 53, pp. 1583–1595.
- 1365 Willmore, C.C., Boudreau, A.E., Spivack, A. and Kruger, F.J., 2002. Halogens of Bushveld
1366 Complex, South Africa: $\delta^{37}\text{Cl}$ and Cl/F evidence for hydration melting of the source
1367 region in a back-arc setting. *Chemical Geology*, 182(2-4), pp.503-511.
- 1368 Wilson, A.H., Zeh, A. and Gerdes, A., 2017. In situ Sr isotopes in plagioclase and trace
1369 element systematics in the lowest part of the Eastern Bushveld Complex: dynamic
1370 processes in an evolving magma chamber. *Journal of Petrology*, 58(2), pp.327-360.
- 1371 Yaxley, G.M., Brey, G.P., 2004. Phase relations of carbonate-bearing eclogite assemblages
1372 from 2.5 to 5.5 GPa: implications for petrogenesis of carbonatites. *Contributions to
1373 Mineralogy and Petrology*, 146(5), pp. 606-619.
- 1374 Zeh, A., Ovtcharova, M., Wilson, A.H., Schaltegger, U., 2015. The Bushveld Complex was
1375 emplaced and cooled in less than one million years - results of zirconology, and
1376 geotectonic implications. *Earth and Planetary Science Letters*.
- 1377 Zeh, A., Wilson, A.H., Gudelius, D., Gerdes, A., 2020. Hafnium Isotopic Composition of the
1378 Bushveld Complex Requires Mantle Melt–Upper Crust Mixing: New Evidence from
1379 Zirconology of Mafic, Felsic and Metasedimentary Rocks. *Journal of Petrology*, 40,
1380 pp. 550–32.
- 1381 Zhang, Z., Lentsch, N. and Hirschmann, M.M., 2015. Carbon-saturated monosulfide melting
1382 in the shallow mantle: solubility and effect on solidus. *Contributions to Mineralogy
1383 and Petrology*, 170(5-6), p.47.
- 1384 Zirakparvar, N.A., Mathez, E.A., Scoates, J.S. and Wall, C.J., 2014. Zircon Hf isotope evidence
1385 for an enriched mantle source for the Bushveld Igneous Complex. *Contributions to
1386 Mineralogy and Petrology*, 168(3), p.1050.
- 1387 Zirakparvar, N.A., Mathez, E.A., Rajesh, H.M., Choe, S., 2019. Lu-Hf isotopic evidence of a
1388 deep mantle plume source for the ~2.06 Ga Bushveld Large Igneous Province. *Lithos*,
1389 348-349, pp. 105-168.

Fig. 1

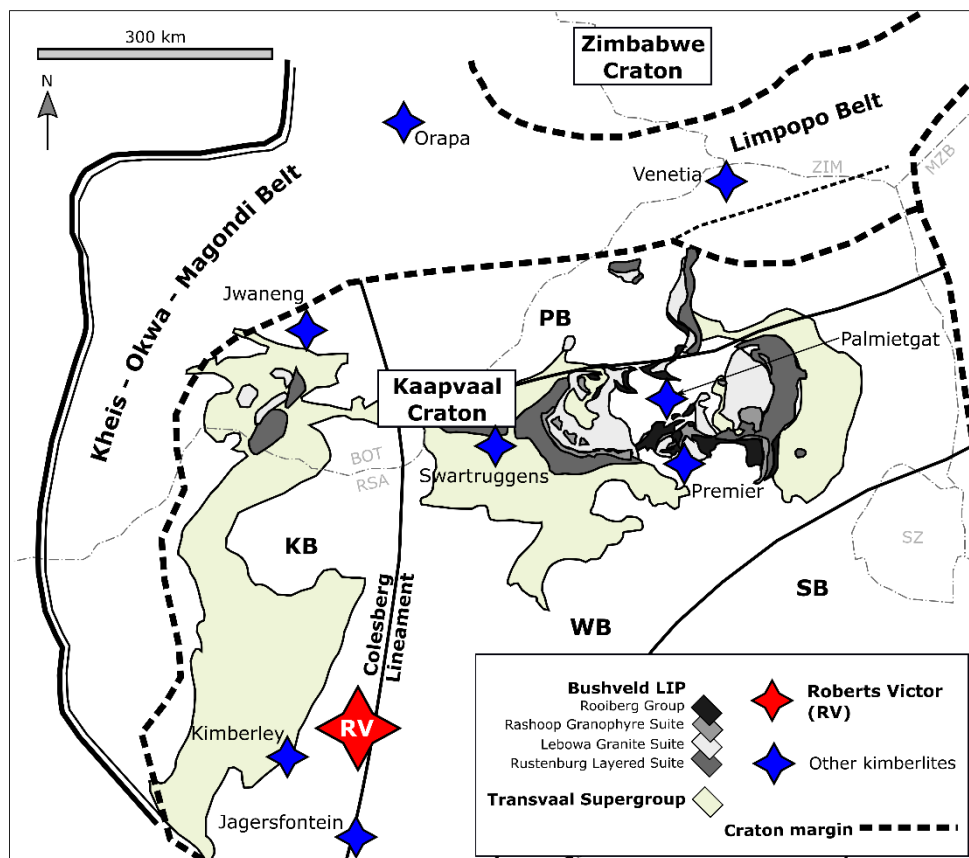


Fig. 2

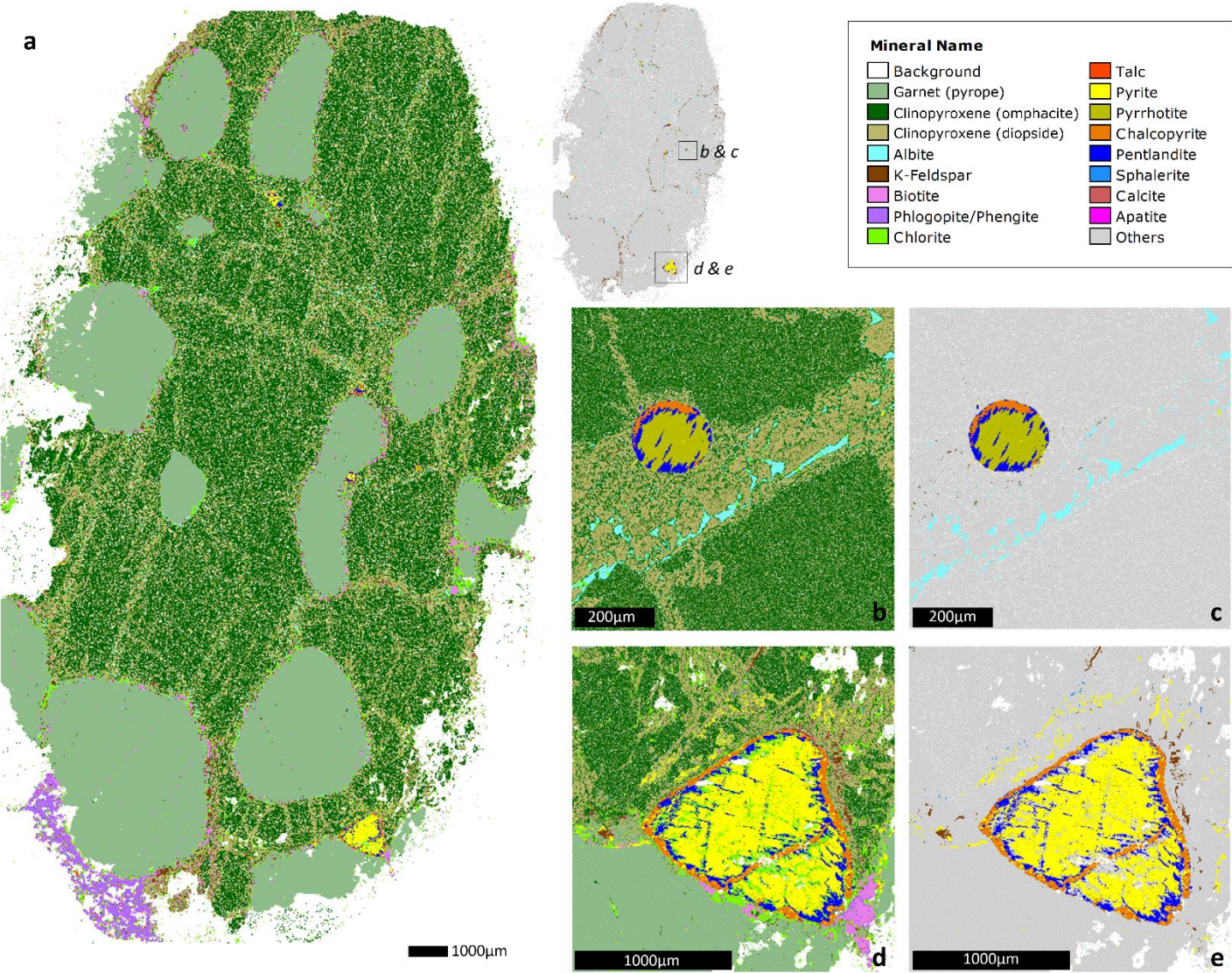


Fig. 3

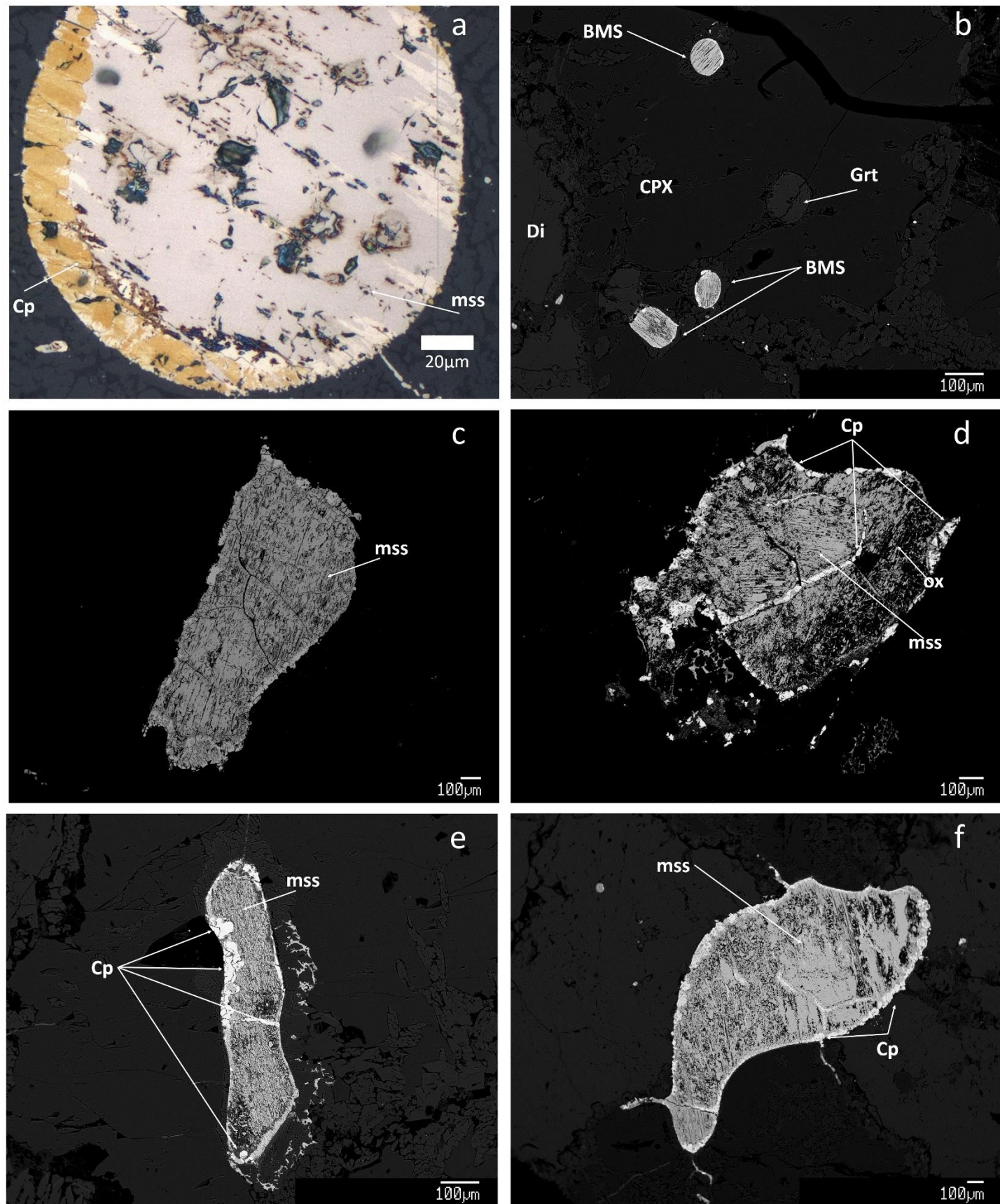


Fig. 4

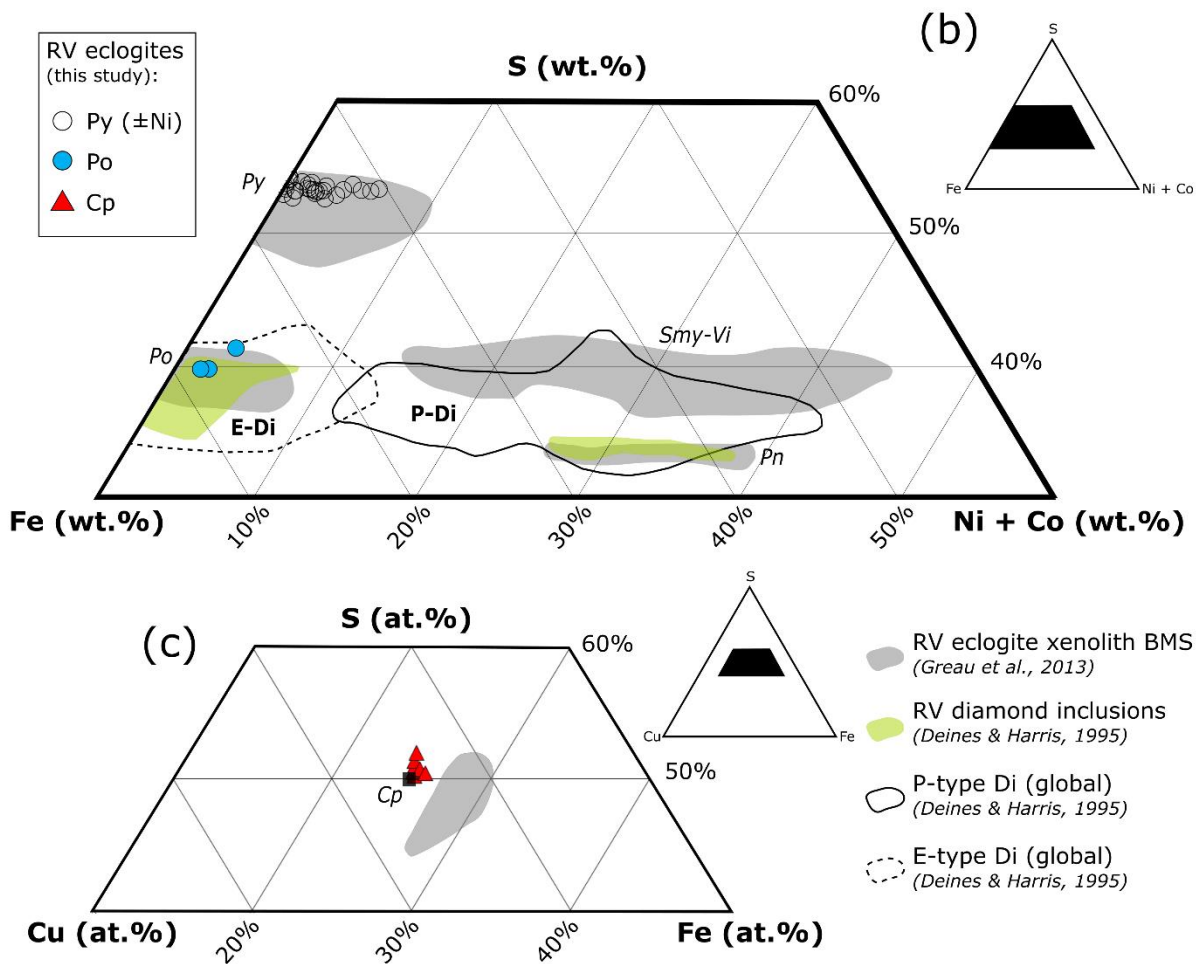
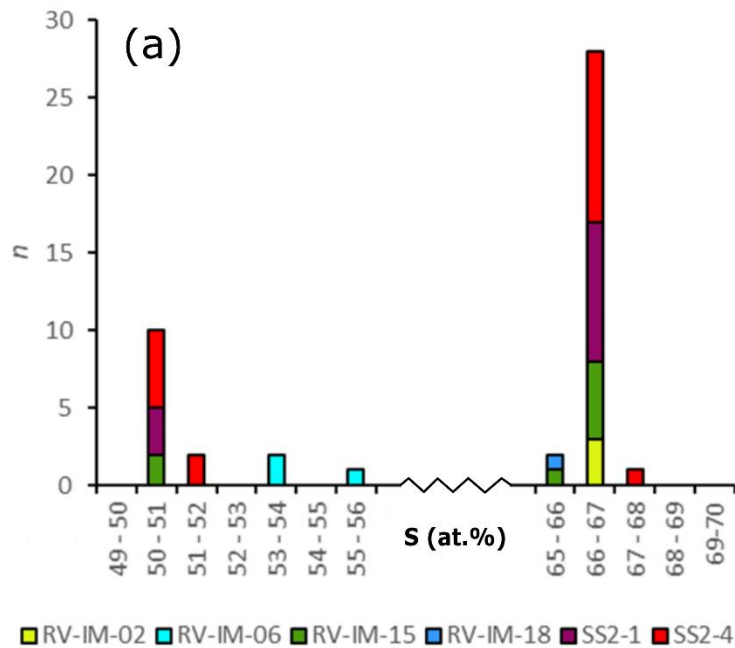


Fig. 5

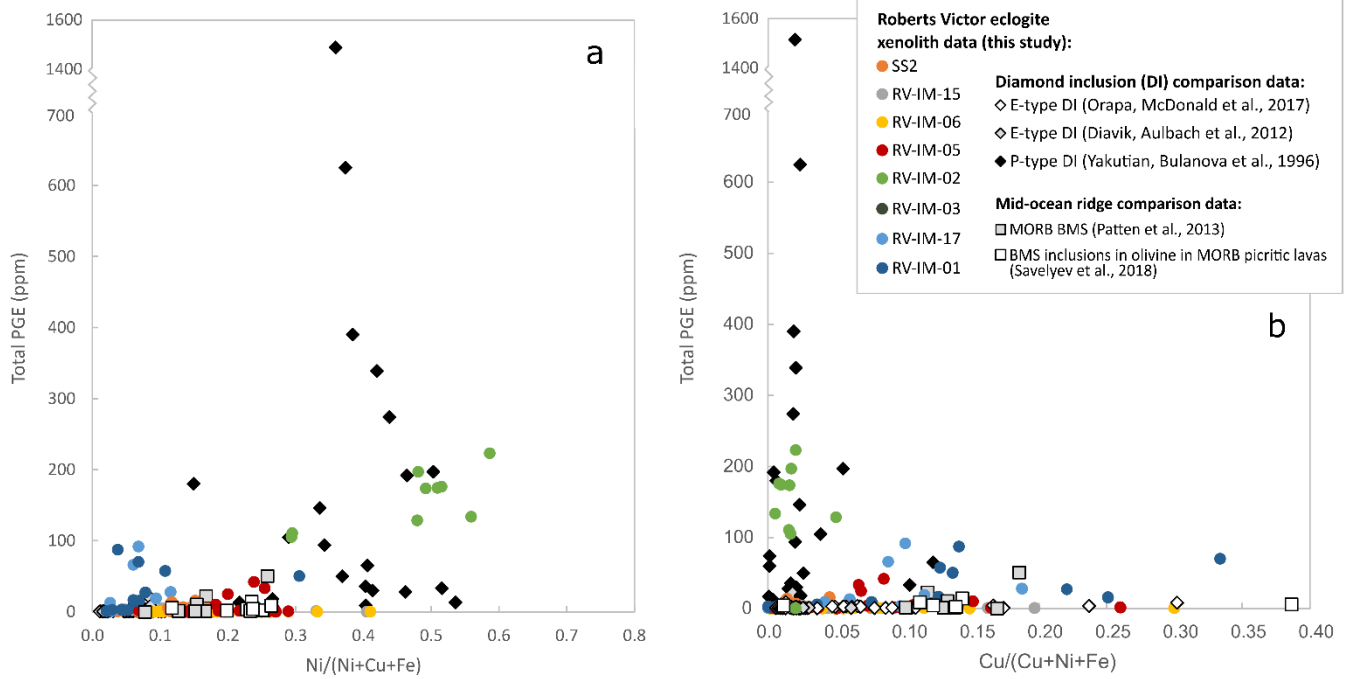
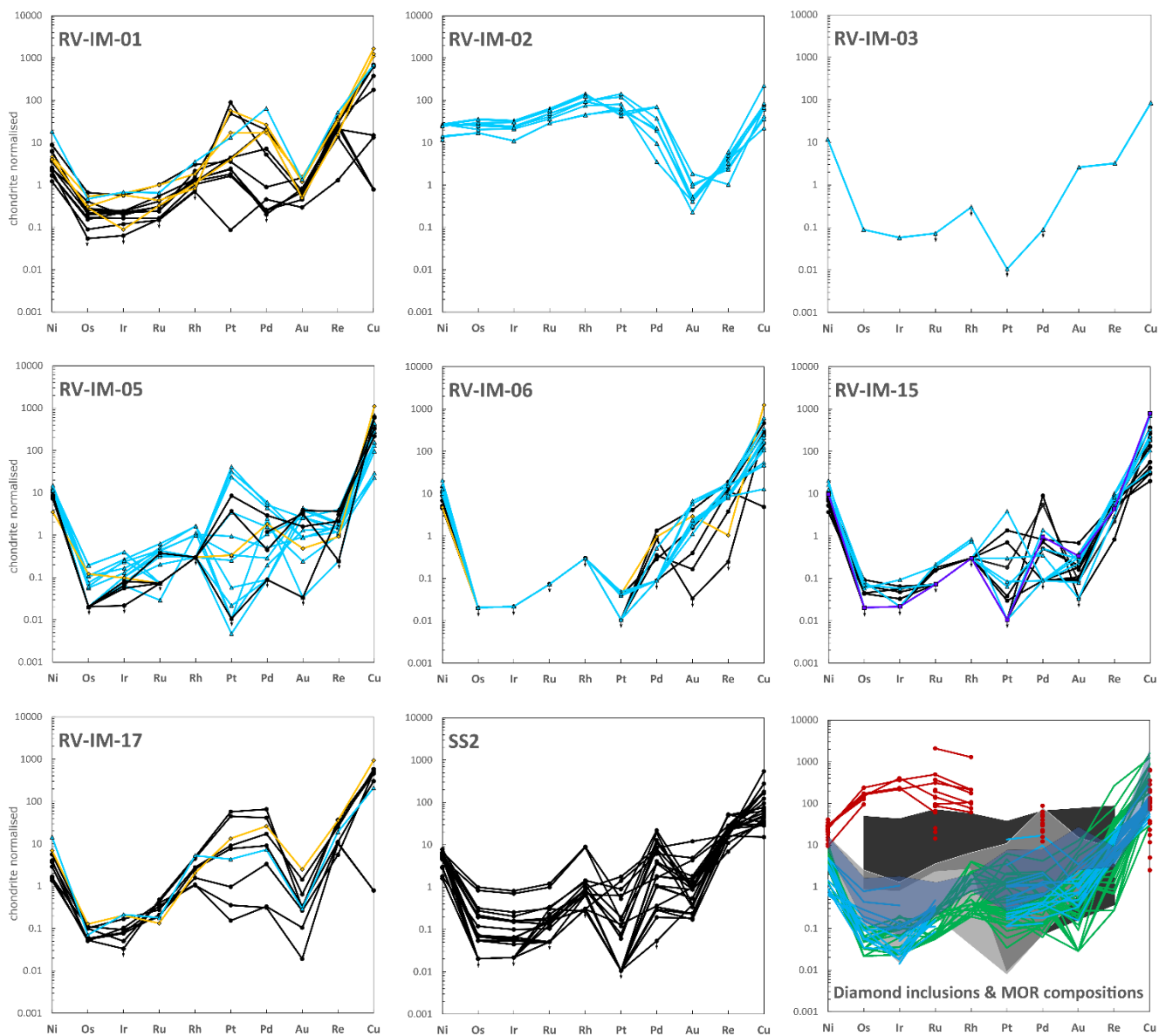


Fig.6



Roberts Victor eclogite xenolith data (this study):
—●— Fe-(Ni,Cu) BMS
—●— Cu,Fe-(Ni) BMS
—▲— Ni,Fe-(Cu) BMS
—●— Ni,Cu,Fe BMS

Mid-ocean ridge data:
■ MORB BMS (Patten et al., 2013)
■ MOR peridotite BMS (Alard et al., 2005)
■ BMS inclusions in olivine (MOR picrite lavas; Savelyev et al., 2018)

Diamond inclusion comparison data:
—●— P-type (Bulanova et al., 1996)
—●— E-type (McDonald et al., 2017)
—●— E-type (Aulbach et al., 2012)

Fig. 7

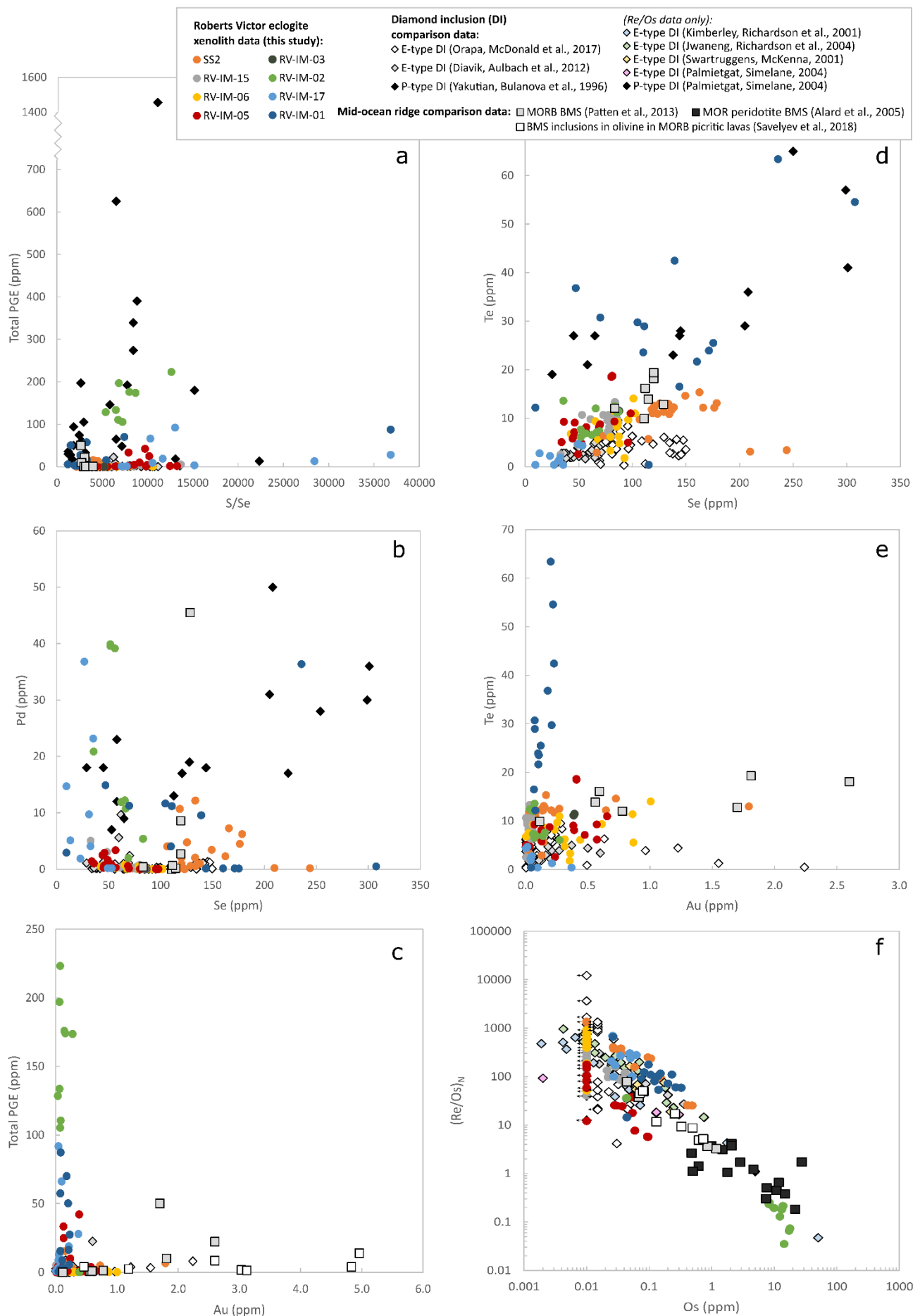


Fig. 8

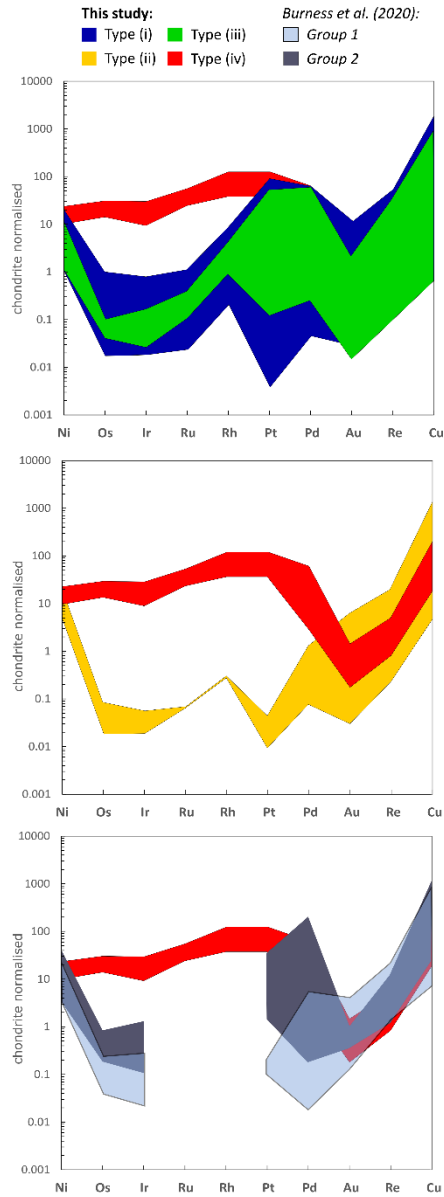


Fig. 9

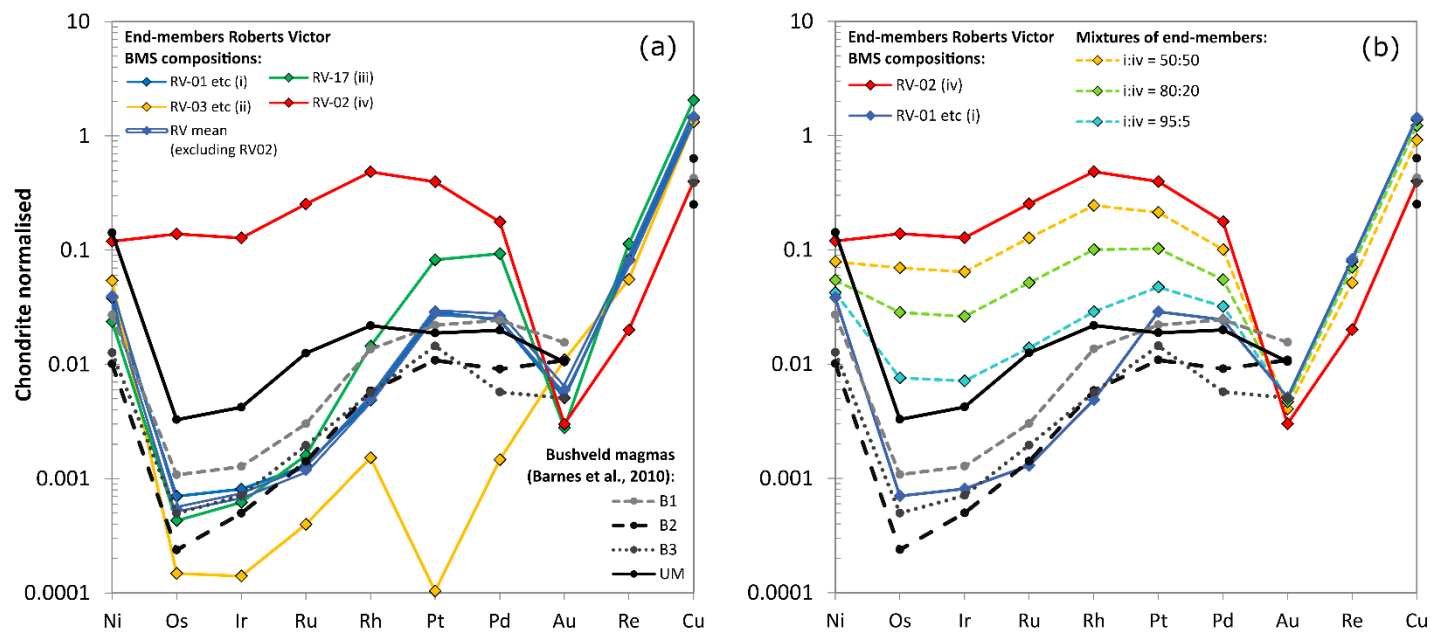


Fig. 10

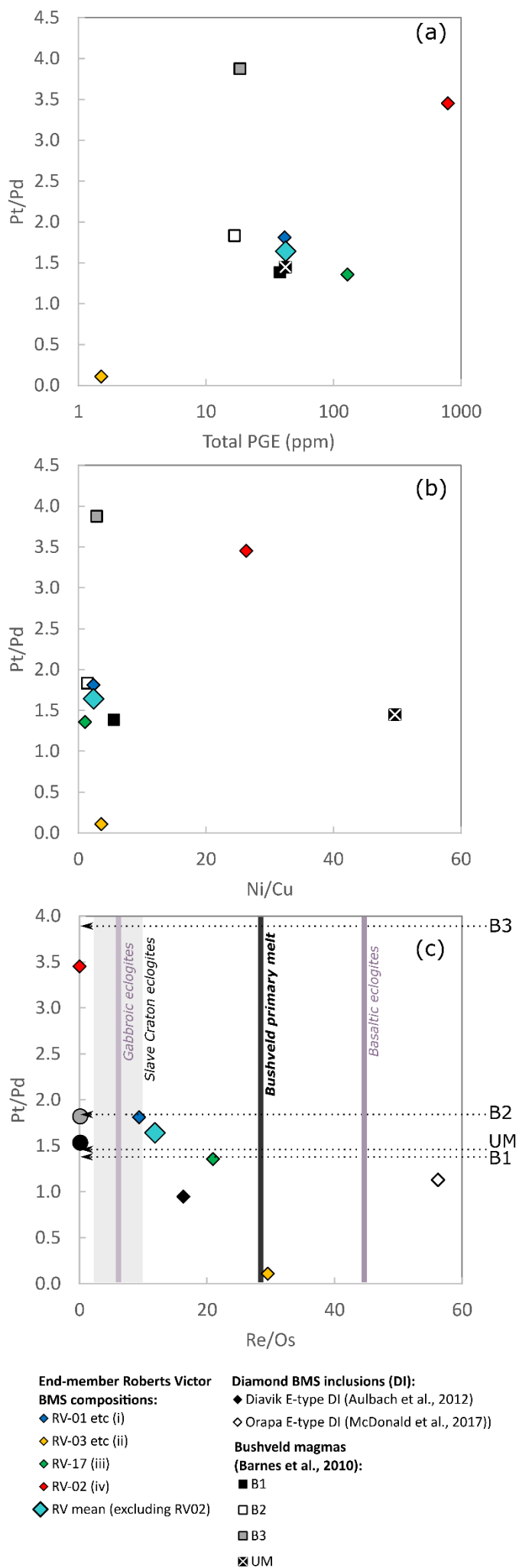


Table 1

Sample #	Modal mineralogy	Petrographic siting of BMS
RV-IM-01	60% CPX, 30% Grt, 5% Phl, 5% accessories (including Chl, Tlc, Alb and KFs, Apt and oxides)	Interstitial
RV-IM-02	50% CPX, 40% Grt, 10% accessories (including Chl, Tlc, Alb and KFs, Apt, Ilm and Rt)	Interstitial
RV-IM-03	-	-
RV-IM-05	60% CPX, 30% Grt, 10% accessories (including Chl, Tlc, Alb and KFs, Apt, Ilm and Rt)	Interstitial
RV-IM-06	25% CPX, 70% Grt, 5% (including Chl, Tlc, Alb and KFs, Apt, Ilm and Rt)	Interstitial & Enclosed
RV-IM-15	50% CPX, 40% Grt, 10% (including Chl, Tlc, Alb and KFs, Apt, Ilm and Rt)	Interstitial & Enclosed
RV-IM-17	-	Interstitial
SS2 *	CPX 50%, Grt 50%, accessory Ilm	Interstitial & Enclosed

Table 2

%	RV-IM-01		RV-IM-15			RV-IM-18	
	*						
Pyrite	70.6	51.6	16.1	51.2	68.5	63.0	21.7
Pyrrhotite	1.9	0.1	-	0.1	0.6	5.0	-
Chalcopyrite	12.4	41.3	42.4	8.5	5.7	7.4	22.1
Pentlandite	15.1	7.0	41.5	40.2	25.2	24.7	56.2

Table 3

Sample	Mineral	n		S	Fe	Ni	Cu	Co	Total	S	Fe	Ni	Cu	Co
				(wt%)						(at%)				
RV-IM-02	Py (\pm Ni)	3	mean	53.19	44.92	0.66	0.45	0.15	99.37	66.77	32.39	0.45	0.29	0.10
			2 σ	0.63	0.99	0.96	1.07	0.17	0.62	0.67	0.73	0.66	0.68	0.11
RV-IM-06	Po	3	mean	40.14	56.77	2.43	< LLD	0.11	99.46	54.15	43.98	1.79	< LLD	0.08
			2 σ	1.59	3.44	1.42	-	0.13	0.51	1.88	2.86	1.04	-	0.10
RV-IM-15	Cp	2	mean	35.29	30.17	0.24	33.75	0.08	99.53	50.54	24.82	0.19	24.39	0.06
			2 σ	0.11	0.11	0.25	0.25	0.01	0.71	0.15	0.06	0.19	0.03	0.01
RV-IM-15	Py (\pm Ni)	6	mean	52.91	45.66	0.71	0.12	0.13	99.52	66.42	32.92	0.49	0.07	0.09
			2 σ	1.06	1.56	1.18	0.21	0.14	1.00	0.63	0.99	0.81	0.13	0.10
RV-IM-18	Py (\pm Ni)	1	-	52.09	43.78	3.00	0.08	0.20	99.15	65.92	31.82	2.07	0.05	0.14
SS2	Cp	10	mean	35.40	30.24	0.14	33.52	0.08	99.36	50.72	24.89	0.11	24.24	0.06
			2 σ	1.11	0.74	0.17	0.69	0.09	0.64	1.07	0.74	0.14	0.66	0.07
	Py (\pm Ni)	21	mean	53.20	43.93	2.20	0.26	0.30	99.86	66.58	31.57	1.51	0.17	0.21
			2 σ	0.88	3.29	3.42	0.56	0.33	1.02	0.46	2.30	2.35	0.35	0.22

Table 5

Sample	n	Interstitial (%)	Included (%)
RV-IM-02	2	100	-
RV-IM-03	2	100	-
RV-IM-05	4	100	-
RV-IM-06	9	11	89
RV-IM-15	8	75	25
SS2	53	89	11
Total	78	79	21

Table 4

Sample	Analysis #	n	33S (wt%)	S/Se	Fe (wt%)	Co (ppm)	Ni (wt%)	Cu	Zn (ppm)	As	Se	Ru	Rh	Pd	Ag	Cd	Sb	Te	Re	Os	Ir	Pt	Au	Bi	
SS2	All (Pv ± Ni)	mean	53.5	4185	39.21	2840	5.42	1.25	17	198	138	0.15	0.18	2.83	3.48	1.32	3.54	10.51	1.00	0.08	0.06	0.25	0.24	0.21	
		σ	-	1302	1.92	616	1.68	1.48	16	201	39	39	0.20	0.32	3.43	6.27	1.92	3.28	3.61	0.47	0.12	0.10	0.45	0.38	0.10
RV15	Pn and Ni-rich BMS (> 10 wt.% Ni)	mean	45	6105	35.69	5125	13.53	4.14	365	406	76	0.07	0.06	0.25	8.13	4.7	9.16	9.75	0.27	0.02	0.02	0.51	0.04	0.36	
		σ	-	1186	4.62	1554	3.91	3.47	257	334	12	0.04	0.03	0.28	4.09	2.7	4.56	2.08	0.10	0.01	0.01	0.01	1.26	0.02	0.18
RV15	Fe-rich BMS ± Ni (< 10 wt.% Ni)	mean	45	6959	44.61	3413	7.48	1.58	117	1634	71	0.06	0.04	1.05	5.42	1.4	13.80	7.86	0.20	0.02	0.02	0.02	0.25	0.03	0.16
		σ	-	2797	2.78	1033	2.11	1.56	101	630	18	0.03	0.00	0.00	1.78	1.71	0.6	4.05	2.68	0.09	0.01	0.01	0.44	0.03	0.11
RV06	Cp	mean	45	5658	31.77	2823	5.08	15.80	174	8	80	0.05	0.04	0.54	3.15	8.0	9.68	6.10	0.04	0.01	0.01	0.04	0.44	0.24	
		σ	-	-	-	-	-	-	-	-	-	-	-	-	-	-	-	-	-	-	-	-	-	-	
RV06	Pn and Ni-rich BMS (> 10 wt.% Ni)	mean	45	5154	37.18	5406	14.16	2.46	39	17	88	0.05	0.04	0.07	4.31	1.0	11.07	7.64	0.51	0.01	0.01	0.02	0.48	0.81	
		σ	-	656	3.97	2090	3.50	2.30	33	9	10	0.00	0.00	0.08	1.51	0.5	5.75	3.92	0.16	0.00	0.00	0.00	0.01	0.31	0.71
RV05	Pn and Ni-rich BMS (> 10 wt.% Ni)	mean	45	7181	44.34	2335	6.49	2.94	50	6	67	0.05	0.04	0.33	1.62	1.1	4.71	8.23	0.38	0.01	0.01	0.02	0.19	0.65	
		σ	-	2232	4.11	861	1.88	1.88	35	9	19	0.00	0.00	0.29	1.10	0.4	3.87	1.11	0.30	0.00	0.00	0.01	0.02	0.26	0.43
RV05	Cp	mean	45	12492	36.45	2173	3.72	14.13	204	20	36	0.05	0.04	1.03	0.66	3.6	16.93	9.26	0.04	0.06	0.05	0.32	0.07	0.19	
		σ	-	-	-	-	-	-	-	-	-	-	-	-	-	-	-	-	-	-	-	-	-	-	
RV05	Pn and Ni-rich BMS (> 10 wt.% Ni)	mean	45	7635	37.24	5334	12.97	3.07	115	1197	64	0.20	0.09	1.03	4.73	2.0	110.54	9.51	0.06	0.04	0.06	7.96	0.29	0.72	
		σ	-	2507	2.73	820	1.71	2.59	46	632	19	0.14	0.07	1.23	2.15	1.7	34.13	4.61	0.04	0.03	0.06	13.92	0.21	0.74	
RV02	Fe-rich BMS ± Ni (< 10 wt.% Ni)	mean	45	8399	40.36	3420	8.34	5.56	200	4646	59	0.10	0.04	0.65	5.22	2.0	127.05	5.22	0.09	0.01	0.03	2.88	0.32	0.22	
		σ	-	2504	4.61	621	0.80	2.49	71	4492	25	0.10	0.00	0.71	2.83	1.4	37.16	1.96	0.06	0.00	0.00	0.01	3.81	0.25	0.08
RV03	Pn and Ni-rich BMS (> 10 wt.% Ni)	mean	45	7864	27.43	16446	25.10	0.95	98	114	60	31.81	12.69	20.20	12.69	2.4	44.81	8.84	0.15	12.85	10.76	69.72	0.11	1.34	
		σ	-	2084	5.08	7429	5.87	0.75	44	119	13	9.14	4.80	15.39	3.44	1.4	13.03	2.94	0.06	3.48	3.76	32.85	0.07	0.57	
RV03	Pn and Ni-rich BMS (> 10 wt.% Ni)	mean	45	5206	39.15	3851	12.59	1.08	61	451	86	0.05	0.04	0.05	10.34	2.4	14.46	11.25	0.13	0.04	0.03	0.01	0.39	0.25	
		σ	-	71	0.48	45	0.13	0.02	2	5	1	0.00	0.00	0.00	0.11	0.1	0.14	0.13	0.00	0.00	0.00	0.00	0.00	0.00	
RV17	Cp	mean	38	36842	44	4855	7.34	11.92	226	143	10	0.09	0.27	14.72	58.99	11.38	6.84	0.40	1.45	0.06	0.09	12.64	0.37	0.25	
		σ	-	-	-	-	-	-	-	-	-	-	-	-	-	-	-	-	-	-	-	-	-	-	
RV17	Pn and Ni-rich BMS (> 10 wt.% Ni)	mean	36.5	10567	46	12263	15.31	2.68	76	563	33	0.12	0.70	4.09	167.52	3.86	26.18	1.90	0.78	0.03	0.10	4.10	0.04	0.04	
		σ	-	-	-	-	-	-	-	-	-	-	-	-	-	-	-	-	-	-	-	-	-	-	
RV01	Pn and Ni-rich BMS (> 10 wt.% Ni)	mean	36	13362	56	2792	3.17	4.24	58	1040	33	0.23	0.35	11.01	111.23	2.50	14.75	2.30	0.75	0.04	0.04	16.18	0.07	0.26	
		σ	-	7228	3	1209	1.69	3.08	48	598	14	0.08	0.21	13.96	105.35	2.62	4.92	1.75	0.49	0.01	0.02	22.29	0.07	0.31	
RV01	Cp	mean	36.5	5164	42	2309	4.53	16.95	637	181	85	0.40	0.17	11.90	38.62	2.14	36.44	36.66	1.14	0.19	0.20	24.87	0.16	0.18	
		σ	-	2422	3	382	0.35	3.79	231	74	48	0.25	0.07	2.72	26.37	1.04	13.14	5.86	0.45	0.07	0.14	26.40	0.08	0.13	
RV01	Pn and Ni-rich BMS (> 10 wt.% Ni)	mean	36	1527	36	6351	19.51	8.70	670	119	236	0.45	0.47	36.37	130.13	0.74	73.60	63.39	2.11	0.23	0.31	12.46	0.20	0.26	
		σ	-	-	-	-	-	-	-	-	-	-	-	-	-	-	-	-	-	-	-	-	-	-	
RV01	Fe-rich BMS ± Ni (< 10 wt.% Ni)	mean	36	6439	52	1911	3.78	3.56	3189	942	139	0.25	0.19	3.44	26.41	2.01	37.90	23.92	0.99	0.11	0.11	16.40	0.11	0.12	
		σ	-	11424	9	1882	2.67	3.81	7426	1615	80	0.19	0.10	4.74	31.78	3.86	21.26	14.78	0.49	0.09	0.09	29.18	0.06	0.06	

Chalcophile and PGE modelling:

In order to evaluate the PGE budget of the eclogitic SCLM, we calculated the bulk concentration of Ni, Cu, Au, Re and the PGE in a silicate magma produced by partial melting of BMS as represented by Roberts Victor eclogite xenolith and compared this to the bulk rock compositions of parental Bushveld magmas (B1, B2 and B3, after Barnes et al., 2010). This method was chosen for two reasons: (i) eclogite xenoliths are small and thus bulk rock analyses are rare or inappropriate and (ii) chalcophile elements, such as the PGE, are primarily controlled by sulphide minerals during partial melting and fractionation, hence the sulphide composition for PGE is of most relevance when considering mantle reservoir compositions and budgets available during partial melting.

We use a batch partial melting model (after Shaw, 2006) from of:

$$\frac{C_L}{C_0} = 1/D + F(1 - D)$$

where C_L = concentration in liquid, C_0 = initial concentration, F = fraction of melting, and D = bulk distribution coefficient.

This assumes that the eclogite is primarily composed of clinopyroxene and garnet (in equal proportions) and 0.5 volume % BMS (total). This proportion of BMS is based on our observations of the abundance of BMS in Roberts Victor eclogite xenoliths (see main text for further information). For the purposes of this modelling, we do not distinguish between MSS, ISS or any end-member sulphide mineral but instead assume a total BMS composition and model the partial melting of this whole BMS. Partition coefficients of all chalcophile elements were set to 10^{-7} in clinopyroxene and garnet (i.e., highly incompatible). Partition coefficients for chalcophile elements in BMS were as follows (from Mungall and Brenan, 2014): 500 (Ni), 3×10^5 (Os), 1.9×10^6 (Ir), 4.85×10^5 (Ru), 5.91×10^5 (Rh), 3.45×10^6 (Pt), 5.36×10^5 (Pd), 6307 (Au), 800 (Re), 1472 (Cu).

By multiplying the abundance of each mineral by the partition coefficient of each element, a bulk distribution coefficient (D) for each element for the bulk rock was calculated. This D value was then applied to the batch partial melting equation (above). A range of degrees of partial melting (F) were used to calculate the composition of the liquid (C_L) formed through partial melting. The composition of BMS used in models were also varied (ranging the four 'types' of BMS identified in Roberts Victor xenoliths from this study – table below and see main text for more details). These C_L compositions were then used in compositional plots (e.g., Figs. 9 and 10). As these represent bulk liquid compositions, no recalculation of B1, B2 or B3 is necessary. Multi-element diagrams show concentrations normalized to chondrite (normalization values from Fischer-Gödde et al., 2010).

Table of starting compositions (BMS end-members) used in modelling

	Ni <i>(wt.%)</i>	Os <i>(ppm)</i>	Ir	Ru	Rh	Pt	Pd	Au	Re	Cu <i>(wt.%)</i>
Type i	8.00	0.07	0.07	0.16	0.13	5.06	2.79	0.18	0.61	3.44
Type ii	11.35	0.01	0.01	0.05	0.04	0.02	0.17	0.38	0.41	3.18
Type iii	4.98	0.04	0.05	0.20	0.38	14.44	10.65	0.10	0.83	4.92
Type iv	25.10	12.85	10.76	31.81	12.69	69.72	20.20	0.11	0.15	0.95
RV mean (excluding RV-IM-02, Type iv)	8.34	0.05	0.06	0.15	0.13	4.99	3.04	0.21	0.59	3.53